

Modelling and observations of photospheric magnetic helicity

P. Démoulin ^{a,*} E. Pariat ^{b,c,d}

^a*Observatoire de Paris, Meudon, LESIA, UMR 8109 (CNRS), F-92195 Meudon Cedex, France*

^b*NASA Goddard Space Flight Center, Greenbelt MD, USA*

^c*College of Science, George Mason University, Fairfax VA, USA*

^d*Naval Research Laboratory, Washington DC, USA*

Abstract

Mounting observational evidence of the emergence of twisted magnetic flux tubes through the photosphere have now been published. Such flux tubes, formed by the solar dynamo and transported through the convection zone, eventually reach the solar atmosphere. Their accumulation in the solar corona leads to flares and coronal mass ejections. Since reconnections occur during the evolution of the flux tubes, the concepts of twist and magnetic stress become inappropriate. Magnetic helicity, as a well preserved quantity, in particular in plasma with high magnetic Reynolds number, is a more suitable physical quantity to use, even if reconnection is involved.

Only recently, it has been realized that the flux of magnetic helicity can be derived from magnetogram time series. This paper reviews the advances made in measuring the helicity injection rate at the photospheric level, mostly in active regions. It relates the observations to our present theoretical understanding of the emergence process. Most of the helicity injection is found during magnetic flux emergence, whereas the effect of differential rotation is small, and the long-term evolution of active regions is still puzzling. The photospheric maps of the injection of magnetic helicity provide new spatial information about the basic properties of the link between the solar activity and its sub-photospheric roots. Finally, the newest technique to measure photospheric flows are reviewed.

Key words: magnetic fields, magnetic helicity, magneto-hydrodynamic, photosphere, corona, coronal mass ejections

* Corresponding author

Email addresses: Pascal.Demoulin@obspm.fr (P. Démoulin),
epariat@helio.gsfc.nasa.gov (E. Pariat).

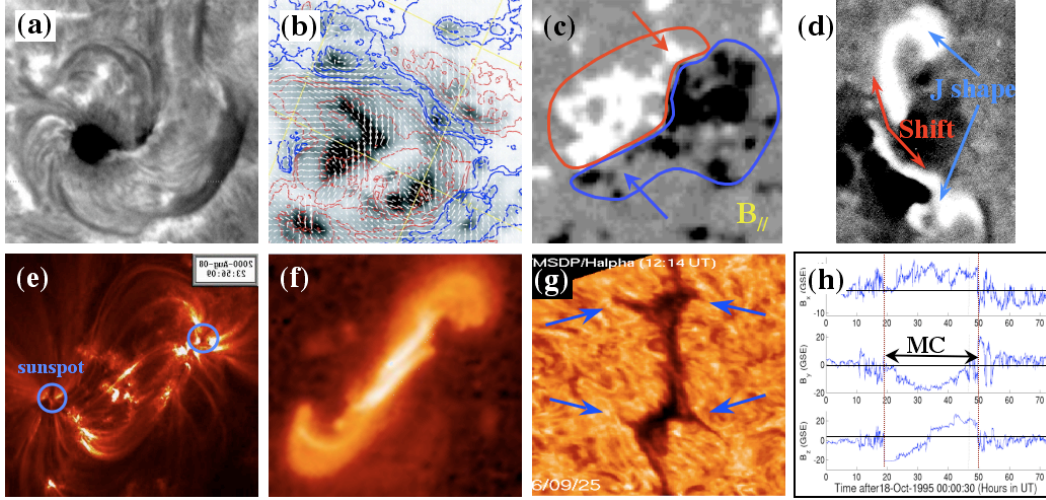


Fig. 1. Evidences of positive magnetic helicity (for negative helicity the images have to be viewed in a mirror). **(a)** Sunspot whorls: spiral pattern of chromospheric fibrils (Hale, 1925; Nakagawa et al., 1971; Chae et al., 2001). **(b)** Vector magnetograms: the presence of magnetic helicity induces a systematic rotation of the observed field compared with the potential state. (Hagyard et al., 1990; Metcalf et al., 2005). **(c)** “Magnetic tongues” in emerging active regions: the asymmetric distribution of the B_n component is interpreted as the contribution of the azimuthal field component of an emerging twisted flux rope (López Fuentes et al., 2000; Green et al., 2007). **(d)** Shift of the flare ribbons along the inversion line. In some flares, two J-shaped ribbons are anti-symmetrically located on both sides of the B_n inversion line : this is an indication of a coronal twist with a number of turn ≥ 1 (Moore et al., 1995; Démoulin et al., 1996). **(e)** Rotating sunspots and sheared coronal loops (Schmieder et al., 1996; Brown et al., 2003). **(f)** Soft X-ray sigmoids: the coronal trace of twisted or highly sheared field lines (Manoharan et al., 1996; Canfield et al., 1999). **(g)** Global organization of fibrils and feet/barbs, i.e. their inclination on the filament axis (Martin et al., 1994; Aulanier et al., 1998). **(h)** Coherent rotation of the magnetic field in magnetic clouds (Bothmer and Schwenn, 1998; Dasso et al., 2006).

1 Why is magnetic helicity important?

Magnetic helicity, noted H , quantifies how much a set of magnetic flux tubes are sheared and/or wounded around each other, with each flux tube contributing proportionally to the square of its axial magnetic flux. In simple examples, H quantifies how much a flux tube is twisted, or how much a magnetic arcade is sheared. However, unlike magnetic shear or twist, magnetic helicity can be precisely defined in complex magnetic configurations (Berger and Field, 1984; Berger and Prior, 2006).

Magnetic helicity has the important property to be very well preserved in plasma having a high magnetic Reynolds number, even taking into account the effects of dissipative processes such as magnetic reconnection. Indeed, H is

almost conserved on a time scale smaller than the global diffusion time-scale (which is defined by the largest spatial scale of the system, Matthaeus and Goldstein, 1982; Berger, 1984). This conservation property is linked to the cascade of H to large spatial scales where dissipative terms are small, whereas magnetic energy cascade to small scales where it is dissipated (Frisch et al., 1975; Alexakis et al., 2006).

The conservation of H defines a constraint to the magnetic field evolution; in particular a stressed magnetic field with finite total helicity cannot relax to a potential field (i.e. a magnetic field without electric currents). Thus magnetic helicity is at the heart of several Magneto-Hydrodynamic (MHD) relaxation theories, for example of coronal heating (e.g. Heyvaerts and Priest, 1984; Vekstein et al., 1993), as well as flares (e.g. Kusano et al., 2004b). Because of this conservation property and the constant injection through the photosphere of magnetic helicity of a given sign in each hemisphere, it has been suggested that Coronal Mass Ejections (CMEs) are needed to avoid the endless accumulation of helicity in the corona (Rust, 1994; Low, 1996). Indeed, Zhang et al. (2006) conjectured the existence of an upper bound on the total magnetic helicity contained by a force free field, given its normal field component at the boundary. They base this conjecture on a series of computed axisymmetric force-free fields. Accumulation of magnetic helicity above this upper threshold would result in a non-equilibrium, eventually resulting in the expulsion of the excess of helicity as a CME. In the convection zone, the accumulation of helicity at large scales limits the efficiency of the dynamo, thus the conservation of magnetic helicity is responsible for the dynamo saturation, the so-called α -effect quenching (Brandenburg and Subramanian, 2005).

Magnetic helicity has remained mostly a theoretical subject for decades (Brown et al., 1999; Berger, 2003). However, the presence of magnetic helicity can be inferred from many phenomena in the solar atmosphere (Fig. 1). Some hemispherical rules have been found for ARs, coronal loops, filaments and magnetic clouds. The hemispherical rules state that helicity is predominantly negative (resp. positive) in the northern (resp. southern) hemisphere. Figure 1 represents the dominant patterns in the southern solar hemisphere, whereas mirrored cases are dominant in the northern hemisphere (e.g. Pevtsov et al., 2008, and references therein). The dominance is independent of the solar cycle and the agreement between the observations and the rules ranges from typically 60-70% for sigmoids to more than 90% for quiescent filaments (see Fig. 4 in Pevtsov, 2002, for a summary). Hemispherical rules in active region also appear when measuring the best fitted α value as well as deriving the current helicity from photospheric vector magnetic field (Pevtsov et al., 2008). However, the distribution of current helicity being of mixed sign (even only considering a simple flux tube having localized twist of a given sign), the results obtained from the current helicity studies, and in particular the level of hemispherical dominance, are not directly comparable to the studies using

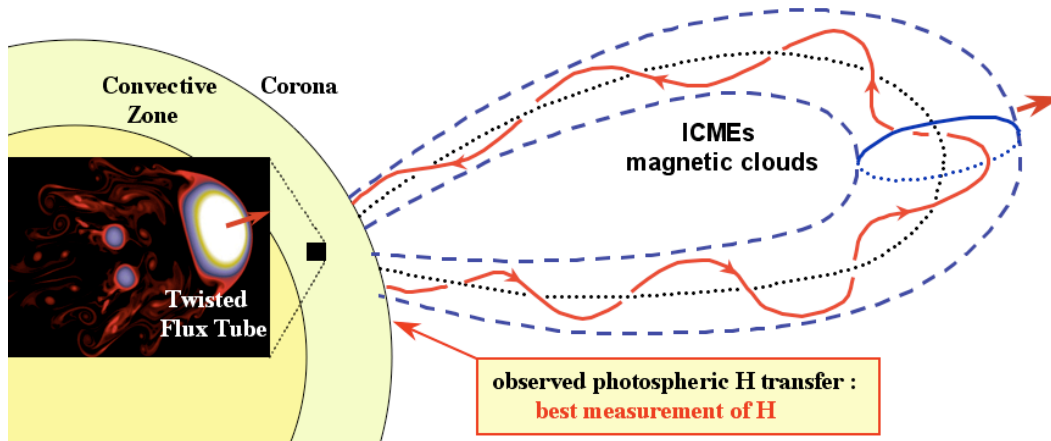


Fig. 2. Schema showing the evolution of magnetic helicity from the convective zone to the interplanetary space. Magnetic flux tubes can cross the convective zone only if they are sufficiently twisted (left insert). After emergence through the photosphere and many transformations (via magnetic reconnection), temporary storage in the corona, the magnetic field and its helicity are launched away via Coronal Mass Ejections (CMEs) detected in the interplanetary space as ICMEs and magnetic clouds (adapted from Cheung et al., 2006).

only the sign of magnetic helicity as a parameter (Démoulin, 2007). Nonetheless, LaBonte et al. (2007) and Yang et al. (2008) found a weak hemispherical dominance ($\approx 57\text{-}60\%$) for the measured photospheric injection of magnetic helicity. The above variety of results shows that the precise magnitude of the hemispherical dominance is still an open subject. It may also indicate that different physical processes may be acting to load/retrieve magnetic helicity in the active Sun compared to the quiet Sun since the hemispherical dominance is significantly larger in the latter.

Very significant advances have been made in the last decade to estimate the magnitude of H in the corona and in the interplanetary space (see Démoulin, 2007, for a review). The amount of H contained in the corona is presently estimated by computations of the magnetic field from observed photospheric magnetograms (so called magnetic field extrapolations). The amount of H launched in a CME is estimated by the change of coronal helicity of the source region during the event. Inside magnetic clouds (one interplanetary consequence of CMEs) H is estimated from in situ measurement of the magnetic field vector. Since only local measurements are available, this requires a flux rope model whose parameters are determined by a least square fit to the data.

Presently, the best determination of H are obtained at the photospheric level since maps of the magnetic field are only available in this region of the solar atmosphere (Fig. 2). More precisely, observations allow us to derive the photospheric rate of magnetic helicity injection. The present paper reviews the advances made by applying the theoretical concepts to temporal series of

photospheric magnetograms. Magnetic helicity and its flux through a surface are first defined in Section 2. Then the results obtained with local correlation tracking are reviewed in Section 3. In addition, not only the total helicity flux (or rate), but also maps of the helicity flux density (or flux per unit surface) can be derived at the photospheric level (Section 4). Furthermore, several new techniques have been recently developed to better estimate the photospheric flows (Section 5). Finally, we briefly conclude in Section 6.

2 Definitions

2.1 Definition of magnetic helicity

Let us consider a generic magnetic field, $\mathbf{B}(\mathbf{x})$, present in the volume \mathcal{V} bounded by the closed surface \mathcal{S} where the normal component of \mathbf{B} , $B_n = \mathbf{B} \cdot \hat{\mathbf{n}}$, can take any value. The definition of the magnetic helicity H of \mathbf{B} requires a reference field \mathbf{B}_p which has the same B_n distribution on the boundary \mathcal{S} than \mathbf{B} (Berger and Field, 1984). A general expression for H is (Finn and Antonsen, 1985):

$$H = \int_{\mathcal{V}} (\mathbf{A} + \mathbf{A}_p) \cdot (\mathbf{B} - \mathbf{B}_p) \, d^3x. \quad (1)$$

The vector potentials \mathbf{A} and \mathbf{A}_p are defined by $\mathbf{B} = \nabla \times \mathbf{A}$, $\mathbf{B}_p = \nabla \times \mathbf{A}_p$ up to a gradient of any scalar function (defining the gauge freedom). By construction H is independent of the gauge selected for \mathbf{A} and \mathbf{A}_p since any change of gauge can only add a term of the form $\nabla \Phi$ to $\mathbf{A} + \mathbf{A}_p$, and the extra integral vanishes because $\nabla \cdot \mathbf{B} = \nabla \cdot \mathbf{B}_p = 0$ and $B_n = B_{p,n}$ on \mathcal{S} .

The freedom in the selection of the gauge of \mathbf{A} and \mathbf{A}_p is typically used to simplify the computations. For example, imposing the same tangential components, $\mathbf{A}_t = \mathbf{A}_{p,t}$, on the boundary \mathcal{S} is compatible with $B_n = B_{p,n}$, and it allows the re-expression of Eq. (1) as a difference of helicities:

$$H = \int_{\mathcal{V}} \mathbf{A} \cdot \mathbf{B} \, d^3x - \int_{\mathcal{V}} \mathbf{A}_p \cdot \mathbf{B}_p \, d^3x. \quad (2)$$

So H appears as a relative magnetic helicity. The potential field being the simplest field, with the lowest magnetic energy, for a given distribution of B_n on \mathcal{S} , it is usually taken as the reference field \mathbf{B}_p .

The current helicity is defined in a similar way as the magnetic helicity, except that it does not need a reference field:

$$H_c = \int_{\mathcal{V}} \mathbf{B} \cdot \mathbf{j} \, d^3x, \quad (3)$$

with $\mu_0 \mathbf{j} = \nabla \times \mathbf{B}$. H_c is not directly measurable in the solar atmosphere (like magnetic helicity, it requires magnetic field extrapolation from photospheric magnetograms). However, the integrand in Eq. (3) can be deduced from vector magnetograms if the field is supposed to be force free (\mathbf{j} being parallel to \mathbf{B}). Without this hypothesis, only the contribution coming from the components normal to the photosphere, $B_n \cdot j_n$, can be derived. This partial determination of the current helicity gives typically a complex pattern of $B_n \cdot j_n$ in ARs, structured at smaller spatial scales than the magnetic field, and presenting a mixture of signs within the same magnetic polarity. However, the global current helicity of ARs follows the hemispherical rules similarly to the other phenomena (Fig. 1), but with one of the weakest agreement ($\approx 60\text{-}70\%$, see Bao et al., 2000; Hagino and Sakurai, 2004, and references therein).

2.2 Flux of magnetic helicity

The changes of the magnetic helicity content within the volume \mathcal{V} is mainly due to helicity flux across \mathcal{S} and a negligible dissipation within \mathcal{V} . In the application to the solar case, \mathcal{V} , is typically a part of the coronal volume, bounded from below by a portion of the photosphere, called \mathcal{S}_p , and bounded in the corona by \mathcal{S}_c ($\mathcal{S}_c = \mathcal{S} - \mathcal{S}_p$). No data can presently provide \mathbf{B} on any \mathcal{S}_c surface. The helicity flux across \mathcal{S}_c can only be estimated indirectly by the helicity carried away by CMEs, and estimated in the interplanetary space from the associated magnetic clouds.

Most of the studies compute the magnetic helicity injected at the photospheric level, through \mathcal{S}_p . The gauge of the vector potential \mathbf{A}_p for the potential magnetic field \mathbf{B}_p is selected to simplify the expression of the helicity flux (or rate), dH/dt (without changing its value, Barnes, 1988; Berger, 1988):

$$\mathbf{A}_p \cdot \hat{n} = 0 \quad \text{on } \mathcal{S}, \quad (4)$$

$$\nabla \cdot \mathbf{A}_p = 0 \quad \text{in } \mathcal{V}. \quad (5)$$

This provides an explicit expression of \mathbf{A}_p , for example when \mathcal{S}_p is a plane,

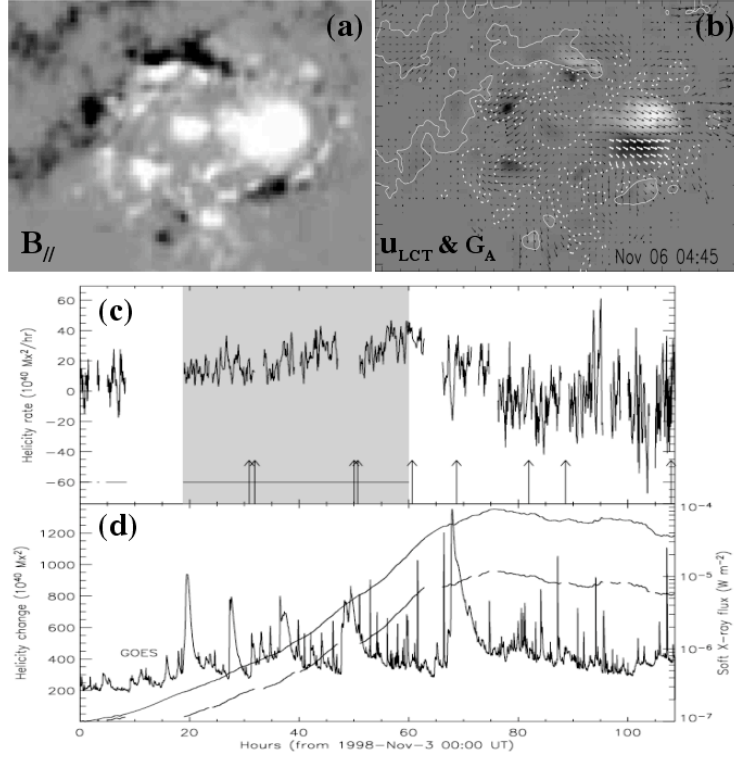


Fig. 3. Magnetic helicity injection in an active region (AR). **(a)** Longitudinal magnetogram of AR 8375 (light/dark levels codes for positive/negative values). **(b)** Photospheric velocity ($\boldsymbol{v}_{\text{LCT}}$, arrows) deduced from Local Correlation Tracking (LCT, Section 2.2) superposed on the helicity flux density, $G_A = -2(\mathbf{A}_p \cdot \boldsymbol{v}_{\text{LCT}})B_n$, distribution (grey-level convention similar to panel (a)). **(c)** Magnetic helicity rate (dH/dt , Eq. (9) with $\mathbf{u} = \boldsymbol{v}_{\text{LCT}}$, or the shearing/twisting term in Eq. (7) with $\mathbf{v}_t = \boldsymbol{v}_{\text{LCT}}$) as deduced from LCT velocity estimations ($\boldsymbol{v}_{\text{LCT}}$). The arrows indicate the time of first detection of each CME launched from AR 8375 (the gray region indicates the time interval when the highest spatial resolution is available for the magnetograms). **(d)** Accumulated change of helicity (lower curve: from the measured dH/dt , upper curve: from a spline interpolation of dH/dt), and full Sun soft X-ray flux (Nindos et al., 2003).

\mathbf{A}_p can be expressed as:

$$\mathbf{A}_p(\mathbf{x}) = \frac{\hat{\mathbf{n}}}{2\pi} \times \int_{S_p} B_n(\mathbf{x}') \frac{\mathbf{x} - \mathbf{x}'}{|\mathbf{x} - \mathbf{x}'|^2} d^2x'. \quad (6)$$

With this gauge of \mathbf{A}_p , the helicity rate dH/dt through a planar surface S_p is (Berger and Field, 1984):

$$\frac{dH}{dt} = 2 \int_{S_p} [\mathbf{A}_p \times (\mathbf{v} \times \mathbf{B})]_n dS,$$

$$= 2 \int_{\mathcal{S}_p} [(\mathbf{A}_p \cdot \mathbf{B}_t)v_n - (\mathbf{A}_p \cdot \mathbf{v}_t)B_n] dS, \quad (7)$$

where \mathbf{B}_t , \mathbf{v}_t , B_n and v_n respectively represent the magnetic field and the plasma velocity tangential and normal to \mathcal{S}_p . The first term in Eq. (7) is usually associated to magnetic flux emergence, whereas the second is associated to shearing/twisting motions.

In addition to magnetograms, plasma velocity maps are needed to estimate dH/dt . Longitudinal velocities, v_{\parallel} , are classically derived from Doppler shift of spectral lines. However, this is not sufficient since the three components of the velocity are needed. Moreover, the measured Doppler velocity is likely to be dominated by the strongest plasma flow component, typically the component aligned with the magnetic field, but which has no contribution to dH/dt (Eq. 7). The method, most widely used so far, to estimate dH/dt is called Local Correlation Tracking (LCT; see Chae et al., 2001, and references therein). The measured velocity, $\boldsymbol{\vartheta}_{\text{LCT}}$, is locally determined by cross correlating a subset (defined by an apodizing window) of two subsequent images shifted by a variable displacement. The measured relative displacement is defined by the shift having the highest correlation; this provides an estimation of the velocity, supposing a uniform motion within the apodizing window. Since the measured velocity is within the plane of the magnetogram, Chae et al. (2001) make the hypothesis that LCT permits an estimate only of the shearing/twisting term in Eq. (7), so $\mathbf{v}_t = \boldsymbol{\vartheta}_{\text{LCT}}$. An example of application to an AR is given in Fig. 3.

2.3 Which helicity rate is measured?

A formal further simplification of dH/dt is realized by defining the velocity \mathbf{u} by:

$$B_n \mathbf{u} = B_n \mathbf{v}_t - v_n \mathbf{B}_t. \quad (8)$$

Then, the photospheric helicity rate simplifies to:

$$\left. \frac{dH}{dt} \right|_{\mathcal{S}_p} = -2 \int_{\mathcal{S}_p} (\mathbf{A}_p \cdot \mathbf{u}) B_n dS. \quad (9)$$

By definition, \mathbf{u} is tangential to \mathcal{S}_p . However, what is the physical interpretation of \mathbf{u} ? If the magnetic field is simply advected (without distortion or reconnection) across \mathcal{S}_p , Démoulin and Berger (2003) have shown that \mathbf{u} is the velocity of the footpoint on \mathcal{S}_p of magnetic flux tubes. If the LCT algorithm is able to track correctly the individual magnetic polarities on \mathcal{S}_p , i.e.

the footpoints of flux tubes, thus $\mathbf{u} = \boldsymbol{\vartheta}_{\text{LCT}}$, and therefore the full helicity rate across \mathcal{S}_p can be estimated.

However, at the photospheric level a sharp stratification of the plasma is present together with a change of physical regime (in particular from high to low β plasma). The crossing of this region by a flux tube forming an AR is difficult since the flux tube is no longer buoyant and it has a larger radius than the local gravitational scale height. The flux tube flattens below the photosphere in a horizontal layer and later, the upper part of the twisted flux tube eventually succeeds to cross the photosphere (e.g., Magara, 2004; Manchester et al., 2004; Murray et al., 2006; Murray and Hood, 2008; Cheung et al., 2008). However, the magnetic dips of the twisted flux tube are loaded by dense material, so that the twisted flux tube is gravitationally anchored to the photosphere in the absence of magnetic reconnection. In fact, observations show that an AR is rather progressively formed by the emergence of a series of thin flux tubes with many reconnections involved before the magnetic field can fill the corona (e.g., Pariat et al., 2004). In this context of complex physical processes involved in the emergence of a twisted flux tube, MHD simulations are needed to test which helicity flux could be detected by methods such as LCT.

So far only one anelastic MHD simulation was used (Welsch et al., 2007; Ravindra et al., 2008; Schuck, 2008). The results, using several methods (see Section 5) including LCT, show that mostly only the shearing/twisting term in Eq. (7) can be determined; so, supporting the original conjecture of (Chae et al., 2001, $\mathbf{v}_t = \boldsymbol{\vartheta}_{\text{LCT}}$). However, this MHD computation does not involve the emergence of a strong and twisted flux tube as observed in the formation of ARs. Indeed, a relatively weak and untwisted magnetic flux tube is initially introduced in a field-free and turbulent model of the top of the convection zone. The flux tube is later distorted and transported at the border of the main simulated convective cell, giving an organization of the plasma flow and magnetic field close to what is observed in super-granules rather than in ARs. The question of which fraction of dH/dt could be measured in ARs, from series of longitudinal magnetograms, thus remains open.

3 Observed photospheric rate

Most of the studies realized so far compute the magnetic helicity injected in ARs with time series of longitudinal magnetograms. The amount of magnetic helicity injected in the coronal field of ARs is typically computed by summing the photospheric rate (Eq. 7) during several days. This section reviews the results obtained with the Local Correlation Tracking (LCT) algorithm. We first discuss the specific input from differential rotation. Then, we present the

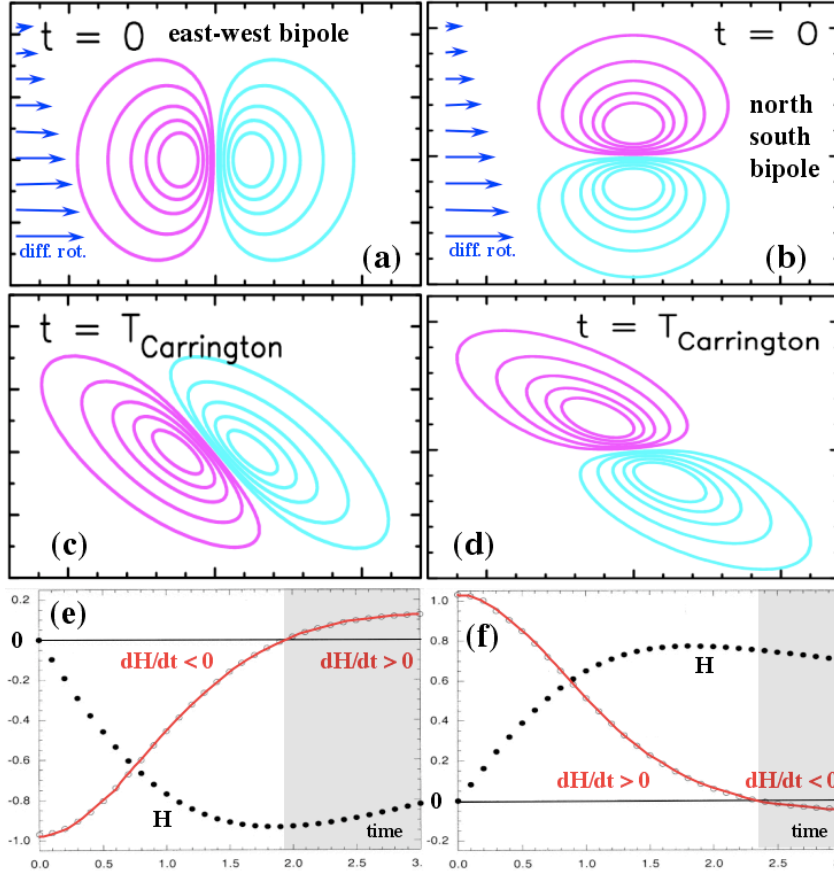


Fig. 4. Temporal evolution of a magnetic bipole initially parallel (left panels) and perpendicular to the equator (right panels) deformed by differential rotation in the northern solar hemisphere. These bipole orientations are typical of young and decayed ARs respectively. Whereas the shearing motion is simple and independent of time, the helicity injection rates (lower panels) are strongly evolving, and even change of sign (shaded regions, DeVore, 2000; Démoulin et al., 2002b).

results of the injection of helicity in ARs during their emergence, peak and decay phases and show that the injection of helicity, presently measured, primarily results from the emergence of twisted structures. We finally summarize the other mechanisms of injections of helicity in ARs.

3.1 Differential rotation

DeVore (2000) first calculated the magnetic helicity injection due to differential rotation. He found that this time-independent shearing flow does not provide a monotonic input of magnetic helicity even for a single magnetic bipole (Fig. 4). Indeed, differential rotation rotates both magnetic polarities on themselves and additionally changes their relative positions, introducing twist and writhe helicity fluxes, respectively. These fluxes always have oppo-

site signs, and have similar amplitude, thereby they partially cancel (Démoulin et al., 2002b). The relative importance of twist and writhe helicity injection by differential rotation depends mainly on the orientation of the bipole (with a change of dominance when the bipole tilt is $\approx 45^\circ$ on the equator). It implies that the input of helicity by differential rotation both depends on time and on the initial orientation of the bipole (see Fig. 4, bottom panels).

In his pioneering work, DeVore (2000) reaches the conclusion that differential rotation can explain the amount of helicity launched in CMEs through a solar cycle. Following studies confirmed the amount of helicity injection found by DeVore, but also show that the pre-SOHO observations were largely underestimating the number of CMEs launched in average by an AR (by a factor ≈ 5 to 10) so that differential rotation is finally not efficient enough to input the needed amount of magnetic helicity. Long-term studies of ARs confirmed it with clearer evidences. Typically the injection of magnetic helicity by differential rotation is a factor 2 to 10 lower than the photospheric helicity rates computed from AR internal motions (deduced from LCT, Chae et al., 2001; Nindos and Zhang, 2002; Nindos et al., 2003; Jeong and Chae, 2007). Even if the input by differential rotation is dominant for a few ARs (e.g. see Table 3 of Nindos et al., 2003), in other ARs differential rotation rather input the opposite sign of magnetic helicity than observed in the corona (Green et al., 2002; Tian and Alexander, 2008). In conclusion, differential rotation is not the main mechanism for injecting magnetic helicity in the corona.

3.2 *Emergence of ARs*

The emergence of an AR, far from any other AR, is typically detected at the photospheric level by the growth and separation of two opposite magnetic polarities. At high spatial resolution, the magnetic field is split in many thin flux tubes which emerge successively. Still the global coherence of the flux tube motions indicates the presence of one main coherent emerging flux tube (which most probably crossed the full convective zone before emerging, see Cheung et al., 2006, and references therein). Such isolated emergence of ARs (e.g. Fig. 5) is best suited to study the intrinsic properties of emerging flux tubes, in particular its magnetic helicity.

3.2.1 *Helicity injection in emerging ARs*

The largest photospheric injection rate of magnetic helicity in ARs is typically found associated to a large increase of the magnetic flux (Figs. 5,6). When the emergence of the AR is monitored from the beginning, a peak in the helicity rate is usually found such as in Fig. 6. The peak of the helicity injection rate

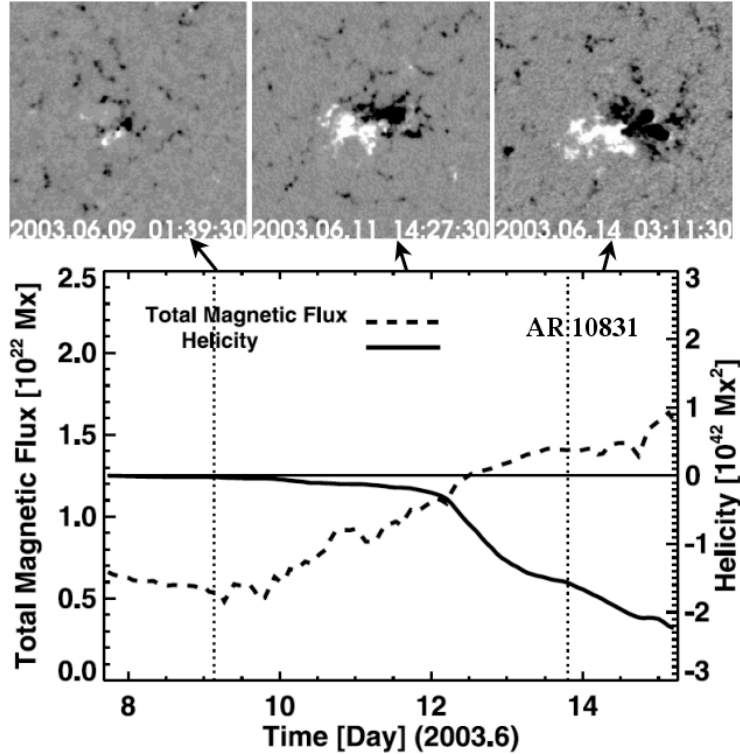


Fig. 5. Helicity injection during the emergence of an AR. The top panels show the longitudinal magnetogram evolution during the beginning of flux emergence. The “magnetic tongues” (Fig. 1c) indicate the emergence of a twisted flux tube with negative magnetic helicity, in agreement with the sign of the injected helicity (continuous line in the bottom panel, scale on the right side). H has a steeper temporal evolution than the magnetic flux (dashed line, scale on the left side, Jeong and Chae, 2007).

is delayed by typically ≈ 2 days relatively to the magnetic flux injection. The initial results obtained with few ARs (Nindos and Zhang, 2002; Chae et al., 2004; Yamamoto et al., 2005), have now been extended to the detailed study of more than 40 ARs (Jeong and Chae, 2007; Tian and Alexander, 2008).

Magnetic emergence is not limited to the growth and separation of the two magnetic polarities since a rotation of the bipole is also observed (e.g. top panels of Fig. 5). The rotation is generally not a true rotation of the magnetic field configuration (but some ARs do have a long term relative rotation of their polarities which is interpreted as the emergence of a writhed flux tube, López Fuentes et al., 2003). This rotation is in fact due for a large part to the evolution of the “magnetic tongues”: they are interpreted as the signature of the azimuthal field component of the emerging flux tube (López Fuentes et al., 2000). These magnetic tongues are present as long as the top part of the twisted flux rope crosses the photosphere (the top part is the region where the flux rope axis is mostly horizontal). The spatial organization of the tongues indicates the sign of the magnetic helicity (negative in Fig. 5 and positive in

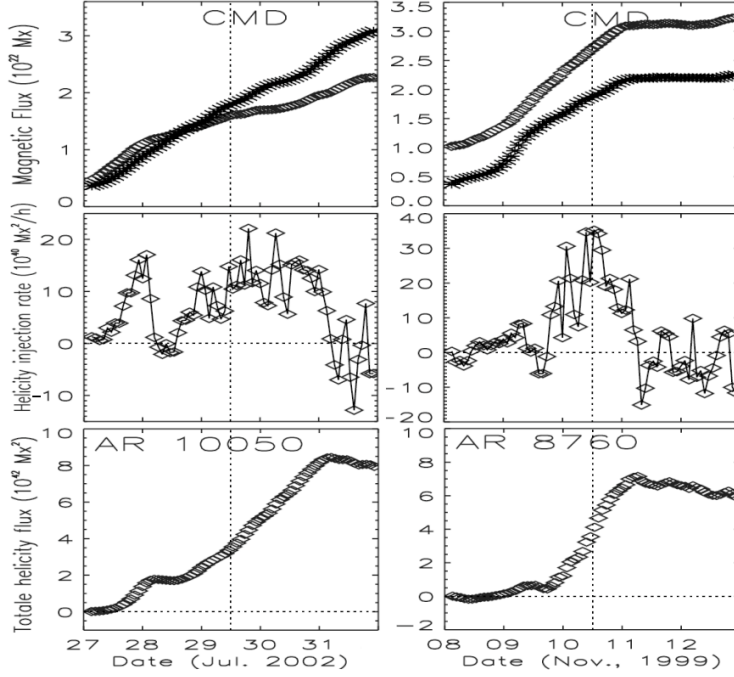


Fig. 6. Absolute magnetic flux of both polarities (top panels), injection rate of magnetic helicity (middle panels), and helicity injected (bottom panels) measured in two emerging ARs. The helicity injection is typically peaked and delayed by ≈ 2 days from the initial magnetic flux increase (Tian and Alexander, 2008).

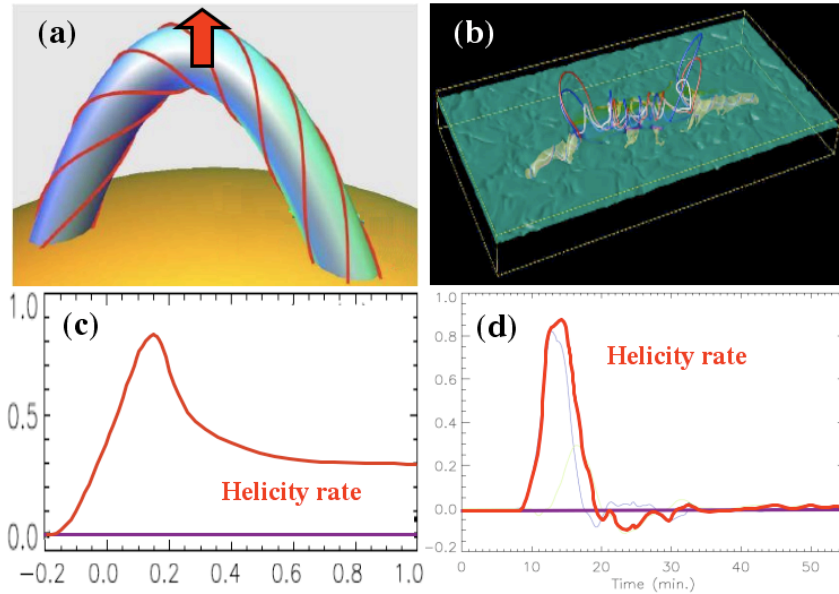


Fig. 7. Injection of magnetic helicity in models of emerging twisted flux tubes. On the left column, the flux rope is simply supposed to move upward with a constant velocity (Pariat et al., 2005). On the right column, an MHD simulation of the emergence across the photosphere is realized (Cheung et al., 2005). In both cases, the helicity injection is qualitatively peaked as in emerging ARs (Fig. 6).

Fig. 1c), independently of the sign of the magnetic polarities.

3.2.2 Helicity injection in models

Models of emerging twisted flux tubes present helicity injection profiles similar to the observations. The simplest model is analytical and considers a magnetic field confined in a torus (Fig. 7, left panels). The field is uniformly twisted, both across and along the flux tube, and half the torus is supposed to cross \mathcal{S}_p with a constant normal velocity. The peak of the helicity injection rate is obtained when the bottom of the top part of the flux tube crosses \mathcal{S}_p (the origin of abscissa in Fig. 7c is when the flux tube axis first crosses \mathcal{S}_p , and the small radius of the flux tube is 0.2, Pariat et al., 2005).

A qualitatively similar peak of helicity injection is found in MHD simulations of emerging twisted flux tubes (Fig. 7, right panels, Cheung et al., 2005, 2008). These simulations solve resistive MHD equations with an extended energy equation including radiative transfer as well as the effect of partial ionization on the equation of state. They found that the emergence term in Eq. (7) contributes to most of the helicity flux during the early stages of emergence, while the shear term becomes more important later when the magnetic field becomes more vertical. This is coherent with the results found by Liu and Zhang (2006) on a fast emerging AR.

The main difference between the simple model and the MHD simulations is the injection rate after the injection peak (compare Fig. 7c,d). In the simple model a significant injection still occurs later because the flux tube legs are still crossing \mathcal{S}_p at the same velocity as the top part had crossed previously \mathcal{S}_p . In reality, a flux tube is no longer buoyant at the photospheric level, and dense plasma accumulates in the magnetic dips of the twisted flux tube, so that the part located below the flux rope axis has difficulties to cross \mathcal{S}_p (see Section 2.3). These effects induce a small injection rate of H as obtained in the MHD simulations.

Indeed the coupling of the convective zone to the corona, through the photospheric region, is a very complex problem still open to investigations (e.g. Moreno-Insertis, 2007). In particular, the fraction of magnetic flux, and to a greater extent of magnetic helicity, initially contained in a buoyant flux rope, which is transferred to the corona remains largely unknown. Most models of the convective zone are largely decoupled from the corona, and inversely for the models of the corona, which usually use boundaries set typically in, or around, the photosphere. Amari et al. (2005) implemented a resistive layer in their MHD simulation to model the thin turbulent photospheric layer and to couple the corona to the convective zone. Even with the extreme case where the vertical component of the plasma velocity is forced to vanish at the top of

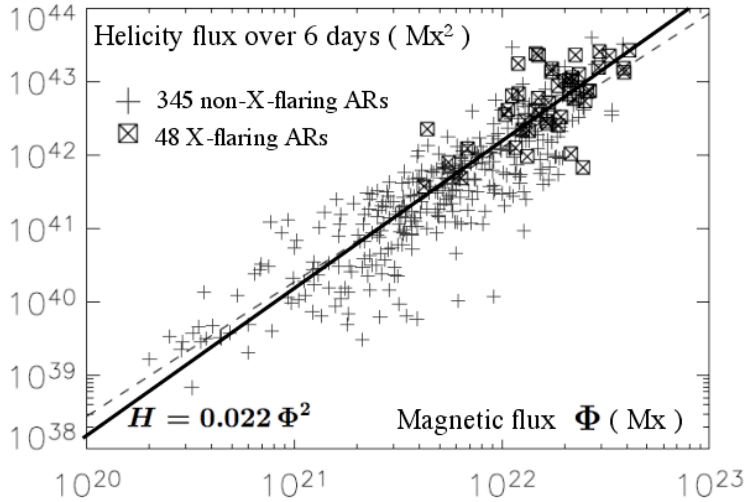


Fig. 8. Magnetic helicity injected in various ARs during 6 days (corresponding to their central disk passage) in function of their magnetic flux (Φ). The best-fit line (dashed) is very close to the solid line giving a flux square dependence. Most X-flare regions have helicity values above 10^{42} Mx^2 (the typical order of magnitude for the helicity launched in a CME, LaBonte et al., 2007).

this photospheric layer, they found that a twisted flux tube progressively succeed to enter in the corona, with an amount of magnetic helicity large enough to lead to a dynamic phase (which could be the initial phase of a CME).

3.2.3 Scaling of the accumulated helicity

The amount of magnetic helicity injected, H_i , in the coronal field of ARs is typically computed by summing the photospheric rate (Eq. 7 or 9) during up to 5-6 days (due to observational constraints). The amount of magnetic flux ranges over a broad domain (about 2.5 decades) and, the values of $|H_i|$ are distributed over an even broader range of values (5 decades, Fig. 8).

Since H is homogeneous to the square of a magnetic flux, it is worth to normalized $|H_i|$ by the average of the absolute value of the magnetic flux Φ crossing the photosphere in both magnetic polarities (and not the absolute sum since the same flux is counted twice). This normalized helicity, $|H_i|/\Phi^2$, also indicates how much the magnetic configuration is stressed since for a flux tube uniformly twisted (both along and across its axis), with n turns, its helicity H is equal to $n\Phi^2$, where Φ is its axial magnetic flux.

A priori, $|H_i|/\Phi^2$ can be any function of Φ (or of another parameter such as the AR size). In fact, the observations show that there is more physics behind the normalization by Φ^2 : Jeong and Chae (2007) found $|H_i| \propto \Phi^{1.3}$ with 6 ARs, a result extended to ≈ 400 ARs by LaBonte et al. (2007) who found $|H_i| \propto \Phi^{1.8}$ (from a least square fit of the data to a straight line in a log-log diagram, see

the dashed line in Fig. 8), and recently confirmed by Yang et al. (2008) who found $|H_i| \propto \Phi^{1.85}$ for 58 emerging ARs. It is remarkable that, in average, $|H_i|/\Phi^2$ has a comparable values for a broad range of ARs. It indicates that small and large ARs are similarly sheared/twisted.

The results of Fig. 8 can still be biased by several effects. Below we discuss two of them, the first effect affects the dispersion around the mean trend and the second changes the slope of the fitted straight line. First, the amount of $|H_i|$ found in an AR, observed during ≈ 6 days around the central meridian, depends on the AR maturity (Figs. 5,6). This effect certainly partly contributes to the scatter present around the best fitted line in Fig. 8. Next, the lifetime of ARs increases significantly with their amount of magnetic flux (Harvey, 1993). This implies that a smaller fraction of the life time of an AR can be observed during 6 days as its magnetic flux is larger. Therefore a smaller fraction of the total helicity, injected during the full duration of an AR, is measured for larger ARs. This effect has the tendency to weaken the exponent of Φ in the best fitted line of Fig. 8, so that the real exponent is expected to be above the value of $1.8 - 1.85$ found.

3.2.4 *Magnitude of the accumulated helicity*

What is the amount of helicity injected? From a sample of 6 ARs (or group of ARs) Nindos et al. (2003) found that $|H_i|/\Phi^2$ lay between ≈ 0.01 and 0.17 . From another set of 6 ARs (including results from Nindos and Zhang (2002) and Liu and Zhang (2006)) Jeong and Chae (2007) determined $|H_i|/\Phi^2$ between ≈ 0.04 and 0.1 . For 18 emerging ARs Tian and Alexander (2008) obtained $|H_i|/\Phi^2 \approx 0.03$, whereas for 23 mature and sigmoidal ARs they found $|H_i| \approx 0.09 + 0.08\Phi^2$ ($|H_i|$ is in units of 10^{44} Mx² and Φ in units of 10^{22} Mx). LaBonte et al. (2007) found the lowest mean value of all the studies: $|H_i|/\Phi^2 \approx 0.02$, a result which could be linked to a larger fraction of old ARs included in their analysis (where less H is injected, see Section 3.3), but also both to the automatic procedure and to the large temporal averaging used (1 day). In summary, the injection of helicity during 5-6 days in ARs, normalized by the square of their magnetic flux, $|H_i|/\Phi^2$, is in the range of a few times 0.01 to a maximum value just above 0.1 . Compared to a twisted flux tube, this is a low amount of twist!

The helicity, H_c , contained at a given time in the coronal field can also be estimated from the magnetic field extrapolation of the photospheric magnetogram, using a model that best fit the observed coronal loops. This provides an estimation independent of the helicity injection computed above (the only common element is a magnetogram at a given time). Within the limits of a linear force-free field extrapolation, Lim et al. (2007) found a maximum value of $|H_c|/\Phi^2 \approx 0.08$ for a large AR whereas Démoulin et al. (2002a), Green et al.

rotation	1	2	3	4	5	6	2-6
AR 7978	11	5	3	5	4	3	20
AR 8100	24	3	12	17	10		42

Table 1

Number of CMEs launched from 2 ARs during each solar rotation (corrected from data gaps). While a larger number of CMEs is launched in the first rotation (including emerging phase) than in any later rotation, more CMEs are still launched after the first rotation (Démoulin et al., 2002a; Green et al., 2002)

(2002), and Mandrini et al. (2005) found a maximum close to 0.2 for two large ARs and one ephemeral region. Taking into account that the injected helicity $|H_i|$, reported in the previous paragraph, is measured over only 5-6 days and in different ARs, the values of $|H_i|/\Phi^2$ found are lower but nonetheless broadly compatible with the independent estimations of $|H_c|/\Phi^2$. Nonetheless, a detailed comparison of the photospheric and coronal measurements for a set of ARs remains to be performed.

Of course, ideally one would like to achieve an helicity budget of the coronal field taking into account the input from the photosphere and the losses in the CMEs (as well as a negligible dissipation). Nindos et al. (2003) and Lim et al. (2007) found that the helicity budget is satisfied in order of magnitude in the few ARs analyzed. In view of the large uncertainties, especially in the helicity transported away by CMEs, it is presently not possible to be more precise.

3.3 Long term evolution of ARs

What is the total amount of magnetic helicity injected in an AR during its full existence? It is presently difficult to completely answer to this question because the injection of helicity can be computed only when the AR is close enough from the central meridian, typically by $\pm 40^\circ$. Therefore a given AR could be observed only less than 1/4 of its existence from instruments at or in the vicinity of Earth. Nevertheless, following the subsequent occurrences of the same AR on the solar disk brings some clues (Fig. 9). The largest injection of H occur during the first rotation, while the injection is small during the second rotation, and negligible later. Jeong and Chae (2007) found this for three ARs analyzed over 2 to 4 solar rotations. This is indeed compatible with the result, reported above, that the most significant helicity injection is associated with new magnetic flux emergence. Without new flux, the magnetic flux of an AR is progressively dispersed by convection to form an enhanced network and this “diffusive” process is not expected to inject magnetic helicity.

The computation of the coronal magnetic field from photospheric magnetograms (called magnetic extrapolation) allows one to estimate the coronal

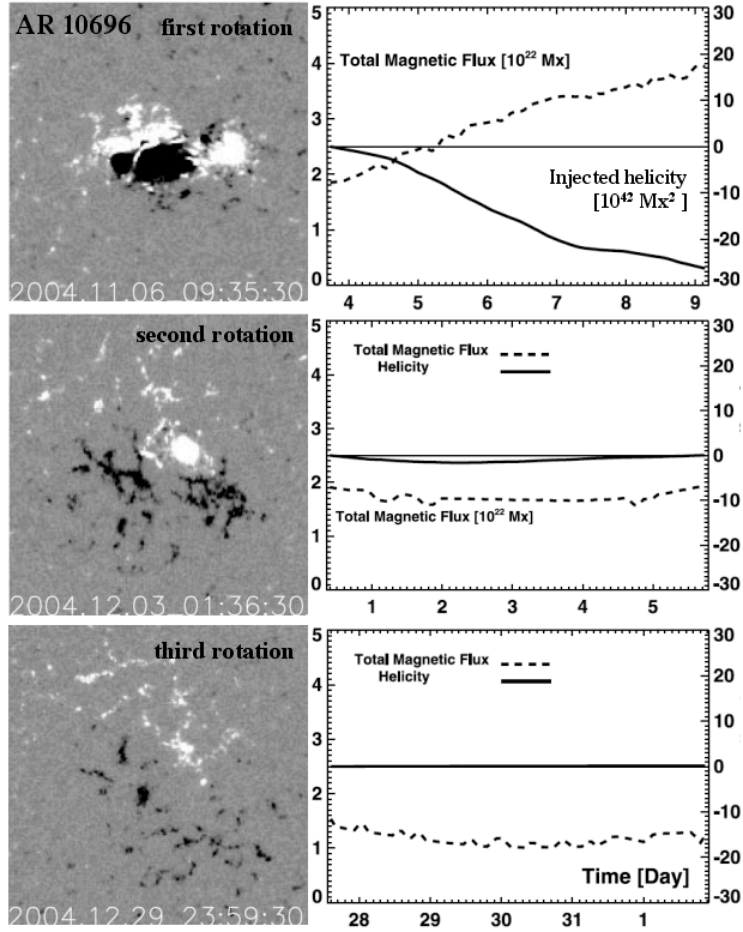


Fig. 9. The same isolated AR followed during 3 solar rotations. The left column shows the evolution and scattering of the longitudinal magnetic field. The right column shows an helicity injection (continuous line) mostly present in the first rotation when the AR magnetic flux is increasing. The scale of the magnetic flux (sum of the absolute flux of both polarities) is on the left side, and the scale of the injected helicity is on the right side (Jeong and Chae, 2007).

helicity, H_c , of an AR. So far the long term evolution of only two isolated and large ARs have been analyzed (using a linear force-free field extrapolation, Démoulin et al., 2002a; Green et al., 2002). $|H_c|$ followed a similar trend for both ARs with a maximum value between the second and third solar rotation (after the AR started emerging), and a progressive decrease later: one fourth of the maximum of $|H_c|$ is reached between the fourth and fifth rotation. *A priori* these results are broadly compatible with the above results on the photospheric injection: the helicity in an AR is predominantly injected during the first month. These results also indicate that ARs keep most of their magnetic helicity for several months.

However, after a CME the AR coronal loops are observed to be less sheared, implying that the coronal magnetic field has lost a significant amount of magnetic helicity. Typically, in one day (sometimes less), the AR coronal loops

are observed to be again significantly sheared indicating a re-loading of H_c . Thus one would expect CMEs to occur mostly when helicity is injected in the coronal field, i.e. principally during the first solar rotation of an AR. Indeed, a larger number of CMEs is launched in the first rotation of both studied ARs (Table 1).

However, the number of CMEs launched from the same AR is about twice larger after the first rotation compared to the first solar rotation! Both studied ARs are still generating a large number of CMEs while $|H_c|$ is only slowly decreasing. Supposing no significant input from the photosphere (as deduced from LCT estimations in other ARs), this may imply that CMEs launched after the first rotation have a low amount of magnetic helicity in order to decrease $|H_c|$ slowly enough. However, this is in contradiction with the magnetic shear evolution of coronal loops from before to just after a CME. Such hypothesis, that CMEs carry less magnetic helicity as the AR decays, has not been reported so far, but is worth to be tested explicitly with observational data. An alternative explanation is that LCT measurements still underestimate the helicity rate, in particular after the emergence phase of ARs. For example during the decay phase, the helicity can be transferred in the corona through torsional Alfvén waves in the multiple flux tubes forming a whole AR (a generalization of the models summarized in Section 3.4, here applied to each individual flux tubes forming the decaying AR).

Finally, ARs cover only a minor fraction of the solar surface. Quiet Sun areas have low magnetic flux density, but they represent a huge amount of the total magnetic flux, so is an important helicity flux also present there? Welsch and Longcope (2003) analyzed five time series of quiet Sun located close to the central disk during the solar minimum. Extrapolating their results to the full Sun, they found that the helicity injection in the quiet Sun is negligible compared to the helicity injected even in a single AR. This result is coherent with the smaller helicity flux rate found in a few ARs as they decay, as summarized above. However, again, the measured helicity rate is probably only the braiding component, and the twist component of individual flux tubes is likely to be missed (since the tiny flux tubes are not well spatially resolved).

3.4 Other mechanisms of magnetic helicity injection

From the works summarized in Section 3.2 and Figs. 5-7 the emergence of sub-photospheric twisted flux tubes appears as the main process for helicity injection. However other processes can be at work, in particular after the emerging phase of ARs and in the quiet Sun, even if they are less obvious to identify in observations.

Longcope and Welsch (2000) and Chae et al. (2003) both proposed a model where most of the twisted flux tube is still present in the convective zone below each AR. It constitutes a reservoir of magnetic helicity for the coronal part. The helicity is transferred by torsional Alfvén waves induced by an imbalance of magnetic torque between the sub-photospheric and the coronal domains. The transfer of helicity is present until the coronal field has a torque large enough to balance the sub-photospheric torque. The main difference between the two models is the assumption for the coronal field; Longcope and Welsch (2000) supposed a linear force-free ($\mathbf{j} = \alpha \mathbf{B}$ with a uniform α value), whereas Chae et al. (2003) supposed a laterally confined flux tube (such as the ones typically considered in the convective zone). Despite the different assumptions, in both cases the increase of the coronal field extension (e.g. via the photospheric magnetic polarity separation) induces a transfer of magnetic helicity from the upper convection zone to the corona.

Chae et al. (2003) tested the above concept with a decaying AR where the spatial extension of coronal loops increase by a factor 2 in 4.5 hours. They deduced from the model an helicity injection of comparable magnitude than the one measured from Eq. (7) using LCT to determined the photospheric velocities. However, it is difficult to observe this process at work in other ARs (Chae, private communication).

Pevtsov et al. (2003) tested the model of Longcope and Welsch (2000) by following the α coefficient (determined by a best fit to coronal loops) in emerging ARs. For the 6 ARs analyzed, $|\alpha|$ is found to grow with the distance separation, d , of the magnetic polarities, and after typically 1.5 day, $|\alpha|$ saturates to a maximum as expected by the model. In fact, the good agreement of the model with the observations is surprising since the model supposes a constant magnetic flux, Φ , of the photospheric polarities whereas the 6 ARs are in the emergence phase. Indeed, the model needs to be extended to the emerging phase (to take into account the Φ evolution), while presently it is more suited for the long-term evolution of ARs, for example to study the reloading of the coronal helicity after the launch of a CME (a research still to be done).

Pevtsov et al. (2003) also found that $|\alpha|$ is growing up together with Φ , in contrast with the observed delay of the helicity injection (see Sect. 3.2 & Figs. 5,6). These results can be qualitatively reconciled using the approximate value of the coronal helicity for a linear force-free bipole: $H \approx \Phi^2 \alpha d / (2\pi)$ (Longcope and Welsch, 2000). Thus, H increases with time not only as Φ^2 , but also with both α and the polarity separation d , so that, as observed, the helicity input is delayed in time compared to Φ^2 .

ARs are typically more complex than a single bipole: magnetic helicity can also be injected through braiding motions. Longcope et al. (2007) used a partitioning technique of a magnetogram (Barnes et al., 2005) to split the injected

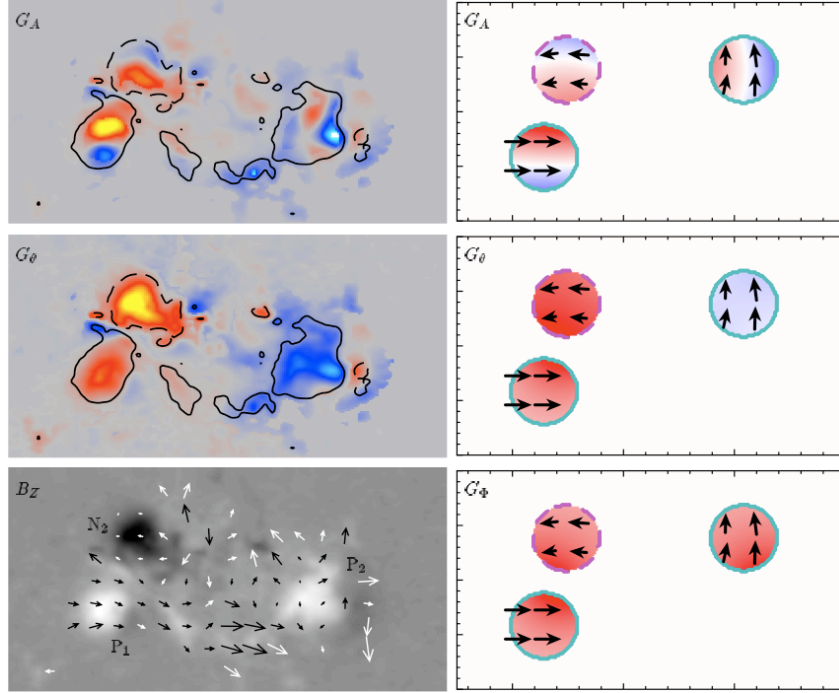


Fig. 10. Comparison of maps with different methods to estimate the helicity flux density in an AR. The temporal evolution of G_A (top row, Eq. 10) and G_θ (middle row, Eq. 12) are shown for AR 9182 (left) and for a model of this AR (right). The bottom left panel shows the longitudinal magnetogram of AR 9182, with LCT velocities (arrows) and polarity labels. The bottom right panel shows the estimation of G_Φ (Eq. 13) for the model. G_A has polarities of both signs, whereas G_θ has mostly the same sign in each magnetic polarities. Similar G_A and G_θ polarities of both signs are present for AR 9182 and its model. However, assuming that the magnetic connectivity of the emerging bipole, N_2P_2 , is kept, G_Φ is everywhere positive. This shows that the negative polarity of G_θ in P_2 is fake (it is due to the relative motion of the nearby magnetic polarities, Pariat et al., 2006).

helicity in twisting and braiding motions. Of course the result depends on the level of splitting of the magnetic polarities (if the splitting is pushed down to elementary flux tubes, then only the braiding of flux tubes contributes to H injection). Longcope et al. (2007) limited the splitting to the main partitions, or “magnetic polarities” (separated from others by weak field). The centroid of the partitions are followed in time, and they found that the centroid velocity is comparable to the corresponding averaged LCT velocity of the same partition. In the 6 ARs studied, both twisting and braiding motions contribute significantly to the helicity injection, so that braiding motions have also to be taken into account in models of magnetic helicity injection.

4 Maps of the helicity flux density

The spatial distribution of the photospheric injection of magnetic helicity has important physical consequences. For example, do we have injection of both signs of magnetic helicity at different location within the same AR? The answer bears consequences for the coronal physics, in particular for flares and CMEs since more magnetic energy can be released when magnetic helicity cancels (e.g. Kusano et al., 2004b). Or is the injection of helicity mostly of a given sign? If it is the case, magnetic helicity accumulates in the corona: can this accumulation finally leads to CMEs? Therefore, in order to answer several key questions of solar physics, the study of the helicity rate is not sufficient and the estimation of the helicity flux per unit surface (called also flux density) is necessary.

4.1 Maps with the vector potential

Equation (9) seems to suggest that the quantity

$$G_A(\mathbf{x}) = -2(\mathbf{A}_p \cdot \mathbf{u})B_n \quad (10)$$

could be a helicity flux density. It has been used extensively to monitor the spatial distribution of magnetic helicity flux in previous studies of ARs (e.g. Chae et al., 2001; Kusano et al., 2002; Nindos et al., 2003; Moon et al., 2002; Liu and Zhang, 2006).

However G_A is non null even with simple flows which do not inject any magnetic helicity in the coronal field! For example, let us consider a vertical magnetic flux tube, with $B_n > 0$, simply translated at a constant velocity \mathbf{u} (say, $\mathbf{u} = U_0\hat{\mathbf{e}}_x$, so here $\mathbf{v}_t = \mathbf{u}$ and $v_n = 0$). In the classical Coulomb gauge ($\nabla \cdot \mathbf{A}_p = 0$), the vector field \mathbf{A}_p is azimuthal (like \mathbf{B} around a current wire). Thus G_A is positive in one half ($y > 0$) of the magnetic polarity, and negative in the other half ($y < 0$) whereas no helicity should be injected! Only the total injection rate (which is null) is correct.

More generally any global motion of flux tubes introduces artificial polarities of both signs in G_A maps. Such fake polarities are typically present in the G_A maps of ARs (e.g. Figs. 3 and 10). Another example, clearly important in solar physics, is the emergence of a flux tube. Pariat et al. (2005) demonstrated that G_A maps, for flux tubes weakly twisted (few 0.1 turn), are fully dominated by negative/positive polarity pairs like in the above examples. The true helicity injection is masked by fake signals, so G_A cannot be used to diagnose the spatial locations of magnetic helicity injection.

4.2 Maps with relative velocities

In order to solve the above problem, \mathbf{A}_p should be explicitly written in terms of the magnetic field (Eq. 6). After some manipulations (see Pariat et al., 2005), Eq. (9) is transformed in:

$$\left. \frac{dH}{dt} \right|_{S_p} = -\frac{1}{2\pi} \int_{S_p} \int_{S_p} \frac{d\theta(\mathbf{x} - \mathbf{x}')}{dt} B_n B'_n d^2x d^2x', \quad (11)$$

with B_n (resp. B'_n) computed at the position \mathbf{x} (resp. \mathbf{x}') and with:

$$\frac{d\theta(\mathbf{x} - \mathbf{x}')}{dt} = \frac{[(\mathbf{x} - \mathbf{x}') \times (\mathbf{u} - \mathbf{u}')]_n}{|\mathbf{x} - \mathbf{x}'|^2}.$$

This implies that the helicity injection rate is the summation of the rotation rate, $d\theta(\mathbf{x} - \mathbf{x}')/dt$, of all the pairs of elementary fluxes weighted by their magnetic flux ($B_n d^2x$). Thus a new estimate of the helicity flux density, called $G_\theta(\mathbf{x})$, is defined by:

$$G_\theta(\mathbf{x}) = -\frac{B_n}{2\pi} \int_{S_p} \frac{d\theta(\mathbf{x} - \mathbf{x}')}{dt} B'_n d^2x'. \quad (12)$$

Considering a magnetic flux tube simply translated at a constant velocity, G_θ is null everywhere, so G_θ does not suffer from the same problem as G_A . For an emerging flux tube, G_θ maps have still some faint fake polarities, but they are apparent only in cases having a low twist (≤ 0.1 turn). Such low twist is not detectable in coronal loop imaging. More generally, studying various examples, the strength of the fake polarities in G_θ maps tends to be at least a factor 10 lower than the G_A 's ones (Pariat et al., 2005, 2007).

In the studied ARs, G_A creates strong fake polarities due to the global motions of magnetic polarities. With G_θ , these spurious signal disappear (Fig. 10): the non-dominant polarities of the helicity flux are suppressed and the intensities of the dominant polarities are lowered (since the total helicity rate is preserved). From the 28 G_θ studied maps, only 3 maps have intense opposite-sign polarities (Pariat et al., 2006). However, in these cases, the patterns are formed primarily by fake polarities due to G_θ (see next section).

The integrations of G_A and G_θ over the full magnetogram should give theoretically the same helicity injection rate (the fake polarities of G_A cancel each others). However there is a difference in the practical applications to magnetograms. The method of Chae et al. (2001) computes \mathbf{A}_p with a fast Fourier transform of the magnetogram. This implies an implicit periodicity of the

magnetic flux distribution whereas the computation of G_θ and its spatial integration supposes that no magnetic flux is present around the magnetogram. The integration of G_A typically over-estimates the injection of helicity between 10% and 30% compare to the integration of G_θ (as \mathbf{A}_p is enhanced by the periodicity, Chae, 2007; Jeong and Chae, 2007).

4.3 Maps with coronal connectivities

Although G_θ is of great practical use, it is still not the flux density of magnetic helicity. Indeed to define it one needs the coronal connectivities of all the elementary flux tubes. Only the helicity rate in each elementary flux tube has a physical meaning. Nevertheless, one can represent this helicity rate in conventional photospheric maps by distributing the helicity input between the two footpoints for each elementary flux tube. In the absence of other information, the natural choice is to split the helicity flux equally between the two footpoints (more generally, it implies that the helicity flux density is still not defined uniquely). The helicity flux can be rewritten as a flux of magnetic helicity per unit surface, called G_Φ (Pariat et al., 2005). G_Φ is a field-weighted average of G_θ at both photospheric footpoints, \mathbf{x}_\pm , of the coronal connection:

$$G_\Phi(\mathbf{x}_\pm) = \frac{1}{2} \left(G_\theta(\mathbf{x}_\pm) + G_\theta(\mathbf{x}_\mp) \left| \frac{B_n(\mathbf{x}_\pm)}{B_n(\mathbf{x}_\mp)} \right| \right). \quad (13)$$

G_Φ was used to remove the remnant fake polarities present with G_θ in the case of an AR emerging nearby to another one (Fig. 10). Strongly contrasting with G_A maps, G_θ maps have a uniform sign over most of studied ARs. In the particular case of AR 9182, the different sign of G_θ in one magnetic polarity disappears when G_Φ is used. We concluded that magnetic helicity density has a coherent sign through each studied AR (in contrast to the mixed sign found for current helicity density). This result needs to be tested on a larger number of ARs. If confirmed, it provides a constraint on solar dynamo models since they would need to explain the formation of twisted flux tubes with either positive, either negative magnetic but not mixed helicity (at the spatial scales resolved by observations).

5 New methods to determine photospheric flows

The different methods to infer velocities from time series of magnetograms have been previously reviewed (Démoulin, 2007; Welsch et al., 2007), so within the present paper, after a short summary of the Local Correlation Tracking

(LCT) principles, we limit ourselves to the description of the most recent advances.

5.1 Local correlation tracking

The LCT method assumes that the photospheric magnetic field is advected by large scale flows, i.e. that flows have not significant variation across the apodizing window selected to perform the cross-correlation. LCT gives an approximate solution to the advection equation:

$$\frac{\partial B_n}{\partial t} + \mathbf{u} \cdot \nabla_t B_n = 0, \quad (14)$$

with ∇_t the gradients tangential to \mathcal{S}_p . LCT determines the average velocity of \mathbf{u} , called $\boldsymbol{\vartheta}_{\text{LCT}}$, over the apodizing window, and it is designed to follow characteristic features which are frozen in the flow. The features are supposed to be not significantly deformed within the time step used to compute $\partial B_n / \partial t$. In the photosphere, these features could be tiny flux tubes. LCT, as all other techniques, works better with a higher number of features to follow per unit area, so with higher resolution data.

However, the magnetic evolution is given by the induction equation. Neglecting any dissipation terms, its normal component to the photosphere is:

$$\frac{\partial B_n}{\partial t} = -\nabla_t \cdot (B_n \mathbf{u}), \quad (15)$$

where \mathbf{u} is related to the plasma velocity by Eq. (8). Even assuming $\mathbf{u} = \boldsymbol{\vartheta}_{\text{LCT}}$, LCT solves a transport equation (Eq. 14) which is different from the one governing the ideal evolution of the photospheric magnetic field (Schuck, 2005).

5.2 Methods solving the ideal induction equation

Equation (15), as Eq. (14), is only a scalar equation for an unknown velocity vector with two components, so the problem of finding the velocity from a series of magnetograms is under-determined. The partial information provided by Eq. (15) on the determination of \mathbf{u} is best seen when the two-dimensional vector $B_n \mathbf{u}$ is written with the Helmholtz's decomposition (Amari et al., 2003):

$$B_n \mathbf{u} = -\nabla_t \phi + \nabla_t \psi \times \hat{n}. \quad (16)$$

Thus, Eq. (15) provides an equation for ϕ alone:

$$\Delta_t \phi = \frac{\partial B_n}{\partial t}, \quad (17)$$

where Δ_t is the Laplacian on the surface \mathcal{S}_p , and $\partial B_n/\partial t$ is computed from the magnetogram time series. It implies that only the $\nabla_t \phi$ term in Eq. (16) can be derived directly from the data! The second term, with ψ , gives the rotational contribution of $B_n \mathbf{u}$, which is the most effective to inject magnetic helicity. Indeed Amari et al. (2003) obtained:

$$\left. \frac{dH}{dt} \right|_{\mathcal{S}_p} = -2 \int_{\mathcal{S}_p} \psi B_n d\mathcal{S}. \quad (18)$$

Welsch et al. (2004) solved this difficulty by taking $\nabla_t \times$ of Eq. (16) to derive a Laplacian equation for ψ , and supposed that $\mathbf{u} = \mathcal{D}_{\text{LCT}}$ in this equation for ψ . It implicitly includes in the method the known limitations of the LCT algorithm. Kusano et al. (2002, 2004a) developed an iteration procedure to solve the induction equation, minimizing the input of the LCT to the velocity component orthogonal to \mathbf{B}_t (thus this method requires vector magnetograms).

The above methods, and some more recent ones (see next sub-sections), were tested with the outputs of an ANMHD simulation of the top of the convection zone (Welsch et al., 2007). A series of synthetic magnetograms were extracted from the simulation results and used with different algorithms to compute the flows, and others physical quantities like the helicity injection rate, similarly to what would be done with real observations. Welsch et al. (2007) also defined a series of tests to quantify how each method deviates from the known results of the simulation. The method which performed best with most (but not all) tests was the MEF method (Longcope, 2004, see next section). But even more importantly, this collective work outlines the weakness of each method and stimulates further developments, as summarized in the two next sub-sections. The new methods have also been tested with the same ANMHD simulation and the same tests, allowing a direct measure of the achieved improvements.

5.3 Minimum energy fit

The minimum energy fit method (MEF) satisfies the ideal induction equation for observed series of magnetogram at each pixel (Longcope, 2004):

$$\frac{\partial B_n}{\partial t} = \nabla_t \cdot (v_n \mathbf{B}_t - B_n \mathbf{v}_t). \quad (19)$$

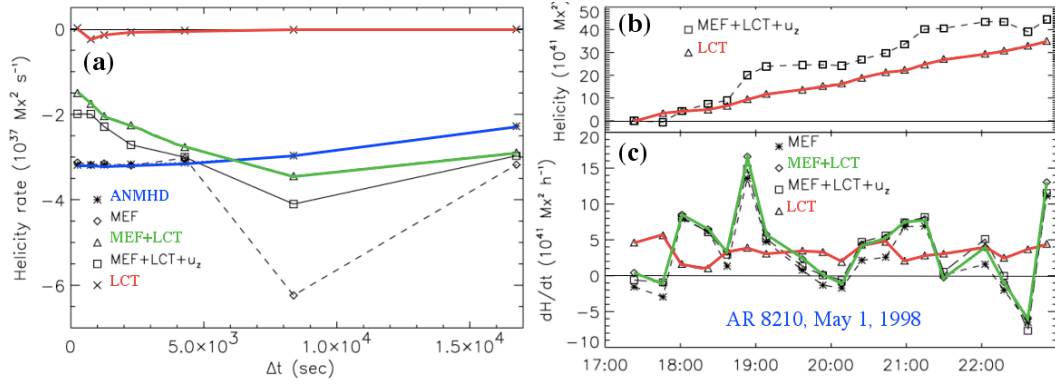


Fig. 11. **(a)** Test of the different versions of the MEF method (Section 5.3) with an ANMHD numerical simulation. The helicity rate is plotted in function of the laps of time Δt selected to compute the evolution of the magnetic field ($\partial B_n / \partial t$) from theoretical magnetograms separated by Δt . **(b,c)** Application of various versions of the MEF method to an AR. The differences in the helicity rate are smaller than in the tests with the numerical simulation (Ravindra et al., 2008).

Equation 19 is similar to Eq. (15), but with \mathbf{u} explicitly written in function of the plasma velocity components (Eq. 8). Since both \mathbf{B}_t and B_n are present in Eq. (19), vector magnetograms are required. The induction equation is also solved using the Helmholtz's decomposition:

$$B_n \mathbf{v}_t = v_n \mathbf{B}_t - \nabla_t \phi + \nabla_t \psi \times \hat{n}. \quad (20)$$

with ϕ the solution of Eq. (17) as described in Sect. 5.2. Then v_n and ψ are computed by minimizing the kinetic energy of $\mathbf{v} - \mathbf{w}$, where \mathbf{w} contains known information on the plasma flow. More precisely, Longcope minimizes the functional:

$$W = \frac{1}{2} \int_{S_p} ((\mathbf{v}_t - \mathbf{w}_t)^2 + (v_n - w_n)^2) dS, \quad (21)$$

under the variation of ψ and v_n , \mathbf{v}_t being replaced by its expression given by Eq. (20).

One advantage of MEF is that it computes a velocity \mathbf{v} compatible with the induction equation and can include partial velocity information in \mathbf{w} from other sources whenever available. When a component of \mathbf{w} is not available, it is set to zero; it implies that the method tends to underestimate the determined velocity. The flexibility of MEF was used by Ravindra et al. (2008) to test several procedures with the ANMHD simulation output used previously by Welsch et al. (2007). They compared the results obtained first with $\mathbf{w} = 0$ (labeled MEF in Fig. 11), second with $\mathbf{w}_t = \boldsymbol{\vartheta}_{\text{LCT}}$ and $w_n = 0$ (MEF+LCT), then with $\mathbf{w}_t = \boldsymbol{\vartheta}_{\text{LCT}}$ and w_n given by the ANMHD simulation (MEF+LCT+ u_z),

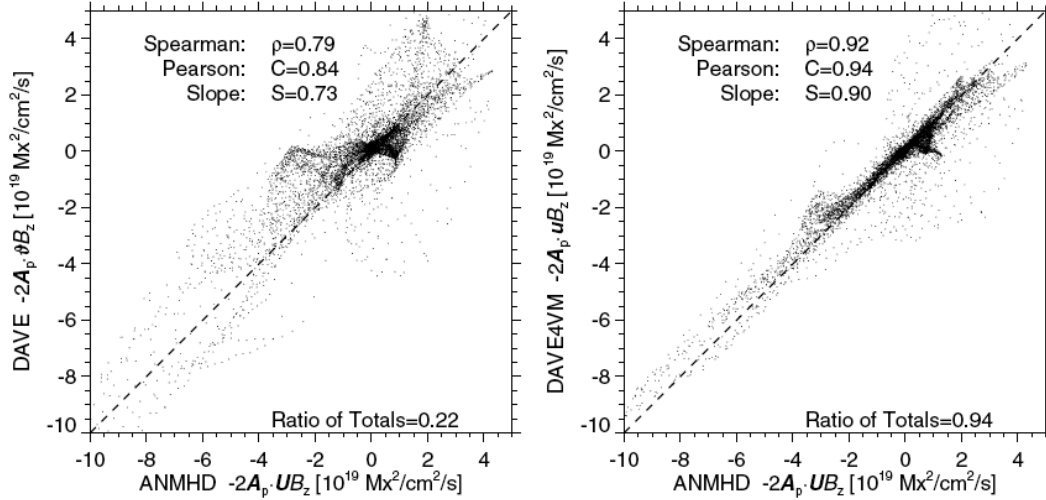


Fig. 12. Test of the DAVE (left) and DAVE4VM (right) with an ANMHD numerical simulation. The scatter plots compare the G_A values (Eq. 10) estimated (in ordinate) to the ones computed directly from the numerical simulation (in abscissa). The quoted values in the panel top are the non parametric Spearman rank-order correlation coefficient, the Pearson correlation coefficient and the slope of the fitted straight line. The ratio of the total helicity fluxes (ratio of the estimated flux over the one computed directly from the simulation) is written at the bottom of each panel. All these measurements show much better results with DAVE4VM than DAVE (Schuck, 2008).

and finally with LCT alone. Figure 11a shows that LCT is unable to find the correct amount of helicity rate, whereas the different implementations of MEF give results much closer to the expected ones (labeled ANMHD). Indeed, in this test, the MEF+LCT results are close to the ANMHD helicity rate for most of the time resolution, Δt , used.

Ravindra et al. (2008) also compared the outputs of the different MEF implementations using a series of vector magnetograms of AR 8210 (an AR very frequently studied, see Section 3 for references). For the method MEF+LCT+ u_z , line-of-sight velocities determined from Dopplergrams are used to input u_z values. Figure 11c shows that the various methods provide much similar flux rates for these observations than the results obtained with the ANMHD simulation (Fig. 11a). Moreover there is not always the same bias (under/over estimation) of the LCT method compared to MEF methods. However, globally, using LCT, slightly less helicity flux is derived compared to other methods (Fig. 11b). This difference of the results shows that the ANMHD simulation is not modeling well enough the dynamic of a typical AR magnetic field (see discussion at the end of Section 2.3).

5.4 Differential affine velocity estimator

Schuck (2005, 2006) designed a method to solve Eq. (15) with finite differences and with a local affine velocity model (allowing linear spatial deformations of the velocity within the apodizing window compared to a uniform velocity for LCT). This method is called the differential affine velocity estimator (DAVE). The determined \mathbf{u} , $\boldsymbol{\vartheta}_{\text{DAVE}}$, satisfies Eq. (15) in a least square sense, providing velocity gradient within the apodizing window (so limiting the decrease of spatial resolution compare to LCT). The least square fit of Eq. (15) to the data provides a robust method which can even be applied to noisy data and allows the use of magnetogram series having a high time cadence (e.g. the method can perform well even when the motions in successive magnetograms are visually dominated by noise). DAVE also provides a quantitative measure of the accuracy of the affine flow model. Schuck (2006) demonstrated that it outperforms the classical LCT approach on synthetic data derived from “moving paint” experiments. Applied to AR 8210, DAVE gives detailed flow patterns which could not be detected by LCT method, in particular a vortex flow is detected intermittently in the main spot. In another AR, Chae (2007) found close results between DAVE and LCT: only 10% more helicity injection with the first one.

As the test with the ANMHD simulation has shown some weakness of DAVE (Welsch et al., 2007), Schuck (2008) extended the method to use vector magnetograms: the new method is called DAVE4VM (DAVE for vector magnetograms). It solves Eq. (19) (rather than Eq. (15) with DAVE), with all plasma velocity components, \mathbf{v}_t and v_n , being described by a local model with linear spatial variations. This *a priori* simple extension, in fact drastically improves the performance of the method for the estimated velocities and the helicity rates (Fig. 12). The improvements come from the explicit presence of the term $v_n \mathbf{B}_t$ in Eq. (19) which cannot be capture by the term $B_n \mathbf{u}$ in Eq. (15) in the ANMHD simulation results. In other words, the evolution of the magnetic flux tubes do not follow the geometrical deformation supposed by Démoulin and Berger (2003). Moreover since the $v_n \mathbf{B}_t$ term is dominant, DAVE (and LCT) cannot determine correctly the plasma flows, as well as the derived quantities such as the helicity flux of the ANMHD simulation.

6 Conclusion

Magnetic helicity, H , is an important global quantity of MHD theory. After having been realized several years ago that H can effectively be estimated in the solar photosphere, in the solar corona and in the interplanetary space from observed data, magnetic helicity received a strong renew of interest. Indeed,

its conservation property is a powerful tool to relate a solar ejection to its interplanetary counter part, independently of the amount of internal magnetic reconnection taking place. This conservation property also provides constraints to the solar dynamo since the amount of magnetic helicity which is observed to cross the photosphere should have been produced below by the solar dynamo. Here also the numerous reconnection events occurring during the photospheric emergence are not expected to significantly change the amount of magnetic helicity. Only the magnetic fields which do not succeed to cross the convection zone (at the periphery of the flux tubes) or which do not succeed to cross the photosphere can induce a deficit in the measured photospheric helicity rate compared to the one generated by the solar dynamo. However, the fraction of magnetic helicity left behind in the convection zone by a flux rope during its main emergence phase is largely unknown, as well as the fraction of this helicity which can later be transferred into the corona during the decaying phase of ARs.

The global solar magnetic field is well organized, following a hemispherical rule which is independent of the solar cycle: negative (resp. positive) magnetic helicity is dominant in the northern (resp. southern) hemisphere. However, these rules are not strong since typically 20-30% of active regions (ARs) have a helicity sign different from the rule. The origin of this weak hemispherical rule is still unknown. Further quantitative studies of magnetic helicity injection in ARs, but also in the quiet Sun, using the new generation of vector magnetograms will certainly help to clarify this issue.

Presently the temporal summation of the helicity rate, measured at the photospheric level, provides the best estimation of the coronal magnetic helicity. The results are coherent with the formation of ARs by the emergence of one global twisted flux tube having a coherent helicity sign. This main flux tube is in fact split in many thin flux tubes at the photospheric level but this does not change significantly the amount and the spatial distribution of magnetic helicity. This result of a uniform sign of H has still to be tested on a much larger number of ARs. If confirmed, the observed photospheric helicity rate in ARs sets a stringent constraint for dynamo models: the dynamo needs to form twisted flux tubes with a given sign of magnetic helicity, with an hemispherical preference, but not a strong one, so that flux tubes of opposite magnetic helicity are partly mixed up in each solar hemisphere! Moreover, the inverse cascade of magnetic helicity to large scales along with the direct cascade of energy to small scales, carrying the opposite sign of magnetic helicity (as found in numerical simulations, see references in Section 1), implies a differentiation of the sign of the magnetic helicity present at different spatial scales. Presently, no observational evidence of such scale separation has been found. In fact, hitherto, it is not certain that we have been able to observe the small scales given the spatial resolution of the observations.

Since time series of longitudinal map are necessary to estimate the helicity flux, developments in photospheric velocity measurements has been stimulated. The latest methods use the richer information obtained from time series of vector magnetograms. This will certainly have an important impact on the quality of the future helicity results, but also in other domains such as the measurements of the inductive electric field and the flux of magnetic energy, important in flare studies for example.

Whereas the status of magnetic helicity has changed from a purely theoretical topic to an observable quantity, with regular input from observations and theoretical studies, several problems remain unanswered. For example, even though an important injection of magnetic helicity is found during the emergence of ARs, it is unknown whether this amount of helicity is sufficient to provide all the magnetic helicity ejected away by the CMEs during the full AR lifetime (including the decay phase of the AR when it is no longer numbered in the NOAA catalog). Another puzzling observation is that quiescent filaments have one of the strongest hemispherical rules. Is it simply because their helicity is the remnant of AR helicity during their dispersion, and only the dominant helicity sign remains (after reconnection between opposite helicity field)? This simple explanation is arguable since quiescent filaments and their magnetic configurations are observed to be ejected as CMEs, living behind a much less sheared configuration which later recovers to a sheared state leading to the formation of a new filament. Where does the magnetic helicity come from then?

Another topic not yet thoroughly studied is the transfer of magnetic helicity, via magnetic reconnection, between different coronal structures. This includes the transfer of H between ARs, even ARs belonging to north/south hemispheres (an evidence being the observed trans-equatorial loops), but also the transfer of H from ARs to the quiet Sun. Moreover, how much magnetic helicity is lost by the corona from the reconnection of closed fields with the open field within coronal holes? Indeed, many interesting questions are still to be addressed benefiting from new methods to measure photospheric flows, from extrapolations of the coronal magnetic field and from the new generation of instruments providing high spatial and temporal resolutions observations (e.g. Hinode, STEREO and soon SDO).

Acknowledgments: We thank the referees and T. Amari for their helpful comments on the manuscript.

References

Alexakis, A., Mininni, P. D., Pouquet, A., 2006. On the Inverse Cascade of Magnetic Helicity. *ApJ* 640, 335–343.

- Amari, T., Luciani, J. F., Aly, J. J., 2005. Non-Current-Free Coronal Closure of Subphotospheric MHD Models. *ApJ* 629, L37–L40.
- Amari, T., Luciani, J. F., Aly, J. J., Mikic, Z., Linker, J., 2003. Coronal Mass Ejection: Initiation, Magnetic Helicity, and Flux Ropes. I. Boundary Motion-driven Evolution. *ApJ* 585, 1073–1086.
- Aulanier, G., Démoulin, P., van Driel-Gesztelyi, L., Mein, P., Deforest, C., 1998. 3-D magnetic configurations supporting prominences. II. The lateral feet as a perturbation of a twisted flux-tube. *A&A* 335, 309–322.
- Bao, S. D., Pevtsov, A. A., Wang, T. J., Zhang, H. Q., 2000. Helicity Computation Using Observations From two Different Polarimetric Instruments. *Sol. Phys.* 195, 75–87.
- Barnes, D. C., 1988. Mechanical injection of magnetic helicity. *Phys. Fluids* 31, 2214–2220.
- Barnes, G., Longcope, D. W., Leka, K. D., 2005. Implementing a Magnetic Charge Topology Model for Solar Active Regions. *ApJ* 629, 561–571.
- Berger, M. A., 1984. Rigorous new limits on magnetic helicity dissipation in the solar corona. *Geophys. Astrophys. Fluid Dyn.* 30, 79–104.
- Berger, M. A., 1988. An energy formula for nonlinear force-free magnetic fields. *A&A* 201, 355–361.
- Berger, M. A., 2003. Topological quantities in magnetohydrodynamics. In: *Advances in Nonlinear Dynamics*. pp. 345–383.
- Berger, M. A., Field, G. B., 1984. The topological properties of magnetic helicity. *J. Fluid. Mech.* 147, 133–148.
- Berger, M. A., Prior, C., 2006. The writhe of open and closed curves. *Journal of Physics A Mathematical General* 39, 8321–8348.
- Bothmer, V., Schwenn, R., 1998. The structure and origin of magnetic clouds in the solar wind. *Annales Geophysicae* 16, 1–24.
- Brandenburg, A., Subramanian, K., 2005. Astrophysical magnetic fields and nonlinear dynamo theory. *Phys. Rep.* 417, 1–209.
- Brown, D. S., Nightingale, R. W., Alexander, D., Schrijver, C. J., Metcalf, T. R., Shine, R. A., Title, A. M., Wolfson, C. J., 2003. Observations of Rotating Sunspots from TRACE. *Sol. Phys.* 216, 79–108.
- Brown, M., Canfield, R., Pevtsov, A., 1999. Magnetic Helicity in Space and Laboratory Plasmas. *Geophys. Mon. Ser.* 111, AGU.
- Canfield, R. C., Hudson, H. S., McKenzie, D. E., 1999. Sigmoidal morphology and eruptive solar activity. *GRL* 26, 627–630.
- Chae, J., 2007. Measurements of magnetic helicity injected through the solar photosphere. *Adv. Space Res.* 39, 1700–1705.
- Chae, J., Moon, Y.-J., Park, Y.-D., 2004. Determination of magnetic helicity content of solar active regions from SOHO/MDI magnetograms. *Sol. Phys.* 223, 39–55.
- Chae, J., Moon, Y.-J., Rust, D. M., Wang, H., Goode, P. R., 2003. Magnetic Helicity Pumping by Twisted Flux Tube Expansion. *J. Korean Astr. Soc.* 36, 33–41.
- Chae, J., Wang, H., Qiu, J., Goode, P. R., Strous, L., Yun, H. S., 2001. The

- Formation of a Prominence in Active Region NOAA 8668. I. SOHO/MDI Observations of Magnetic Field Evolution. *ApJ* 560, 476–489.
- Cheung, M., Schüssler, M., Moreno-Insertis, F., 2005. 3D Magneto-Convection and Flux Emergence in the Photosphere. In: Innes, D. E., Lagg, A., Solanki, S. A. (Eds.), *ESA SP-596: Chromospheric and Coronal Magnetic Fields*. p. 54.1.
- Cheung, M. C. M., Moreno-Insertis, F., Schüssler, M., 2006. Moving magnetic tubes: fragmentation, vortex streets and the limit of the approximation of thin flux tubes. *A&A* 451, 303–317.
- Cheung, M. C. M., Schüssler, M., Tarbell, T. D., Title, A. M., Nov. 2008. Solar Surface Emerging Flux Regions: A Comparative Study of Radiative MHD Modeling and Hinode SOT Observations. *ApJ* 687, 1373–1387.
- Dasso, S., Mandrini, C. H., Démoulin, P., Luoni, M. L., 2006. A new model-independent method to compute magnetic helicity in magnetic clouds. *A&A* 455, 349–359.
- Démoulin, P., 2007. Recent theoretical and observational developments in magnetic helicity studies. *Adv. Space Res.* 39, 1674–1693.
- Démoulin, P., Berger, M. A., 2003. Magnetic Energy and Helicity Fluxes at the Photospheric Level. *Sol. Phys.* 215, 203–215.
- Démoulin, P., Mandrini, C. H., van Driel-Gesztelyi, L., *et al.*, 2002a. What is the source of the magnetic helicity shed by CMEs? The long-term helicity budget of AR 7978. *A&A* 382, 650–665.
- Démoulin, P., Mandrini, C. H., Van Driel-Gesztelyi, L., Lopez Fuentes, M. C., Aulanier, G., 2002b. The Magnetic Helicity Injected by Shearing Motions. *Sol. Phys.* 207, 87–110.
- Démoulin, P., Priest, E. R., Lonie, D. P., 1996. Three-dimensional magnetic reconnection without null points 2. Application to twisted flux tubes. *JGR* 101, 7631–7646.
- DeVore, C. R., 2000. Magnetic Helicity Generation by Solar Differential Rotation. *ApJ* 539, 944–953.
- Finn, J. H., Antonsen, T. M. J., 1985. Magnetic helicity: What is it, and what is it good for? *Comments Plasma Phys. Contr. Fus.* 9, 111–126.
- Frisch, U., Pouquet, A., Leorat, J., Mazure, A., 1975. Possibility of an inverse cascade of magnetic helicity in magnetohydrodynamic turbulence. *J. Fluid. Mech.* 68, 769–778.
- Green, L. M., Kliem, B., Török, T., van Driel-Gesztelyi, L., Attrill, G. D. R., 2007. Transient coronal sigmoids and rotating erupting flux ropes. *Sol. Phys.* 246, 365–392.
- Green, L. M., López fuentes, M. C., Mandrini, C. H., *et al.*, 2002. The Magnetic Helicity Budget of a CME-Prolific Active Region. *Sol. Phys.* 208, 43–68.
- Hagino, M., Sakurai, T., 2004. Latitude Variation of Helicity in Solar Active Regions. *Publ. Astron. Soc. Japan* 56, 831–843.
- Hagyard, M. J., Venkatakrisnan, P., Smith, Jr., J. B., 1990. Nonpotential magnetic fields at sites of gamma-ray flares. *ApJ Sup. Series* 73, 159–163.
- Hale, G. E., 1925. Nature of the Hydrogen Vortices Surrounding Sun-spots.

- Publ. Astron. Soc. Pacific 37, 268–270.
- Harvey, K. L., 1993. Magnetic Bipoles on the Sun. Ph.D. Thesis, Utrecht University.
- Heyvaerts, J., Priest, E. R., 1984. Coronal heating by reconnection in DC current systems - A theory based on Taylor's hypothesis. *A&A* 137, 63–78.
- Jeong, H., Chae, J., 2007. Magnetic Helicity Injection in Active Regions. *ApJ* 671, 1022–1033.
- Kusano, K., Maeshiro, T., Yokoyama, T., Sakurai, T., 2002. Measurement of Magnetic Helicity Injection and Free Energy Loading into the Solar Corona. *ApJ* 577, 501–512.
- Kusano, K., Maeshiro, T., Yokoyama, T., Sakurai, T., 2004a. Study of Magnetic Helicity in the Solar Corona. In: Sakurai, T., Sekii, T. (Eds.), *The Solar-B Mission and the Forefront of Solar Physics*. Vol. 325 of Astronomical Society of the Pacific Conference Series. pp. 175–184.
- Kusano, K., Maeshiro, T., Yokoyama, T., Sakurai, T., 2004b. The Trigger Mechanism of Solar Flares in a Coronal Arcade with Reversed Magnetic Shear. *ApJ* 610, 537–549.
- López Fuentes, M. C., Démoulin, P., Mandrini, C. H., Pevtsov, A. A., van Driel-Gesztelyi, L., 2003. Magnetic twist and writhe of active regions. On the origin of deformed flux tubes. *A&A* 397, 305–318.
- López Fuentes, M. C., Démoulin, P., Mandrini, C. H., van Driel-Gesztelyi, L., 2000. The Counterkink Rotation of a Non-Hale Active Region. *ApJ* 544, 540–549.
- LaBonte, B. J., Georgoulis, M. K., Rust, D. M., 2007. Survey of Magnetic Helicity Injection in Regions Producing X-Class Flares. *ApJ* 671, 955–963.
- Lim, E.-K., Jeong, H., Chae, J., Moon, Y.-J., 2007. A Check for Consistency between Different Magnetic Helicity Measurements Based on the Helicity Conservation Principle. *ApJ* 656, 1167–1172.
- Liu, J., Zhang, H., 2006. The Magnetic Field, Horizontal Motion and Helicity in a Fast Emerging Flux Region which Eventually forms a Delta Spot. *Sol. Phys.* 234, 21–40.
- Longcope, D. W., 2004. Inferring a Photospheric Velocity Field from a Sequence of Vector Magnetograms: The Minimum Energy Fit. *ApJ* 612, 1181–1192.
- Longcope, D. W., Ravindra, B., Barnes, G., 2007. Determining the Source of Coronal Helicity through Measurements of Braiding and Spin Helicity Fluxes in Active Regions. *ApJ* 668, 571–585.
- Longcope, D. W., Welsch, B. T., 2000. A Model for the Emergence of a Twisted Magnetic Flux Tube. *ApJ* 545, 1089–1100.
- Low, B. C., 1996. Solar Activity and the Corona. *Sol. Phys.* 167, 217–265.
- Magara, T., 2004. A Model for Dynamic Evolution of Emerging Magnetic Fields in the Sun. *ApJ* 605, 480–492.
- Manchester, IV, W., Gombosi, T., DeZeeuw, D., Fan, Y., 2004. Eruption of a Buoyantly Emerging Magnetic Flux Rope. *ApJ* 610, 588–596.
- Mandrini, C. H., Pohjolainen, S., Dasso, S., *et al.*, 2005. Interplanetary flux

- rope ejected from an X-ray bright point. The smallest magnetic cloud source-region ever observed. *A&A* 434, 725–740.
- Manoharan, P. K., van Driel-Gesztelyi, L., Pick, M., Démoulin, P., 1996. Evidence for Large-Scale Solar Magnetic Reconnection from Radio and X-Ray Measurements. *ApJ* 468, L73–L77.
- Martin, S. F., Bilimoria, R., Tracadas, P. W., 1994. Magnetic field configurations basic to filament channels and filaments. In: Rutten, R. J., Schrijver, C. J. (Eds.), *Solar Surface Magnetism*. p. 303.
- Matthaeus, W. H., Goldstein, M. L., 1982. Measurement of the rugged invariants of magnetohydrodynamic turbulence in the solar wind. *JGR* 87, 6011–6028.
- Metcalf, T. R., Leka, K. D., Mickey, D. L., 2005. Magnetic Free Energy in NOAA Active Region 10486 on 2003 October 29. *ApJ* 623, L53–L56.
- Moon, Y.-J., Chae, J., Wang, H., Choe, G. S., Park, Y. D., 2002. Impulsive Variations of the Magnetic Helicity Change Rate Associated with Eruptive Flares. *ApJ* 580, 528–537.
- Moore, R. L., Larosa, T. N., Orwig, L. E., 1995. The wall of reconnection-driven magnetohydrodynamic turbulence in a large solar flare. *ApJ* 438, 985–966.
- Moreno-Insertis, F., Oct. 2007. Three-dimensional numerical experiments of flux emergence into the corona. In: Shibata, K., Nagata, S., Sakurai, T. (Eds.), *New Solar Physics with Solar-B Mission*. Vol. 369 of *Astronomical Society of the Pacific Conference Series*. p. 335.
- Murray, M. J., Hood, A. W., Feb. 2008. Emerging flux tubes from the solar interior into the atmosphere: effects of non-constant twist. *A&A* 479, 567–577.
- Murray, M. J., Hood, A. W., Moreno-Insertis, F., Galsgaard, K., Archontis, V., Dec. 2006. 3D simulations identifying the effects of varying the twist and field strength of an emerging flux tube. *A&A* 460, 909–923.
- Nakagawa, Y., Raadu, M. A., Billings, D. E., McNamara, D., 1971. On the Topology of Filaments and Chromospheric Fibrils near Sunspots. *Sol. Phys.* 19, 72–85.
- Nindos, A., Zhang, H., 2002. Photospheric Motions and Coronal Mass Ejection Productivity. *ApJ* 573, L133–L136.
- Nindos, A., Zhang, J., Zhang, H., 2003. The Magnetic Helicity Budget of Solar Active Regions and Coronal Mass Ejections. *ApJ* 594, 1033–1048.
- Pariat, E., Aulanier, G., Schmieder, B., Georgoulis, M. K., Rust, D. M., Bernasconi, P. N., 2004. Resistive Emergence of Undulatory Flux Tubes. *ApJ* 614, 1099–1112.
- Pariat, E., Démoulin, P., Berger, M. A., 2005. Photospheric flux density of magnetic helicity. *A&A* 439, 1191–1203.
- Pariat, E., Démoulin, P., Nindos, A., 2007. How to improve the maps of magnetic helicity injection in active regions? *Adv. Space Res.* 39, 1706–1714.
- Pariat, E., Nindos, A., Démoulin, P., Berger, M. A., 2006. What is the spatial distribution of magnetic helicity injected in a solar active region? *A&A* 452,

- 623–630.
- Pevtsov, A. A., 2002. Sinuous Coronal Loops at the Sun [Invited]. In: Martens, P. C. H., Cauffman, D. (Eds.), *Multi-Wavelength Observations of Coronal Structure and Dynamics*. pp. 125–134.
- Pevtsov, A. A., Canfield, R. C., Sakurai, T., Hagino, M., 2008. On the solar cycle variation of the hemispheric rule. *ApJ* 677, 719–722.
- Pevtsov, A. A., Maleev, V. M., Longcope, D. W., 2003. Helicity Evolution in Emerging Active Regions. *ApJ* 593, 1217–1225.
- Ravindra, B., Longcope, D. W., Abbett, W. P., 2008. Inferring Photospheric Velocity Fields Using a Combination of Minimum Energy Fit, Local Correlation Tracking, and Doppler Velocity. *ApJ* 677, 751–768.
- Rust, D. M., 1994. Spawning and shedding helical magnetic fields in the solar atmosphere. *GRL* 21, 241–244.
- Schmieder, B., Demoulin, P., Aulanier, G., Golub, L., 1996. Differential Magnetic Field Shear in an Active Region. *ApJ* 467, 881–886.
- Schuck, P. W., 2005. Local Correlation Tracking and the Magnetic Induction Equation. *ApJ* 632, L53–L56.
- Schuck, P. W., 2006. Tracking Magnetic Footpoints with the Magnetic Induction Equation. *ApJ* 646, 1358–1391.
- Schuck, P. W., 2008. Tracking Vector Magnetograms with the Magnetic Induction Equation. *ApJ* 683, 1134–1152.
- Tian, L., Alexander, D., 2008. On the Origin of Magnetic Helicity in the Solar Corona. *ApJ* 673, 532–543.
- Vekstein, G. E., Priest, E. R., Steele, C. D. C., 1993. On the Problem of Magnetic Coronal Heating by Turbulent Relaxation. *ApJ* 417, 781–789.
- Welsch, B. T., Abbett, W. P., DeRosa, M. L., Fisher, G. H., Georgoulis, M. K., Kusano, K., Longcope, D. W., Ravindra, B., Schuck, P. W., 2007. Tests and Comparisons of Velocity-Inversion Techniques. *ApJ* 670, 1434–1452.
- Welsch, B. T., Fisher, G. H., Abbett, W. P., Regnier, S., 2004. ILCT: Recovering Photospheric Velocities from Magnetograms by Combining the Induction Equation with Local Correlation Tracking. *ApJ* 610, 1148–1156.
- Welsch, B. T., Longcope, D. W., 2003. Magnetic Helicity Injection by Horizontal Flows in the Quiet Sun. I. Mutual-Helicity Flux. *ApJ* 588, 620–629.
- Yamamoto, T. T., Kusano, K., Maeshiro, T., Yokoyama, T., Sakurai, T., 2005. Magnetic Helicity Injection and Sigmoidal Coronal Loops. *ApJ* 624, 1072–1079.
- Yang, S., Zhang, H., Buechner, J., 2008. Magnetic helicity accumulation and tilt angle evolution of newly emerging simple active regions. In: Hardi, P. (Ed.), *Electronic proceedings of “12th European Solar Physics Meeting”*, <http://espm.kis.uni-freiburg.de>. pp. 2.2–37.
- Zhang, M., Flyer, N., Low, B. C., 2006. Magnetic Field Confinement in the Corona: The Role of Magnetic Helicity Accumulation. *ApJ* 644, 575–586.

Fig. 1. Evidences of positive magnetic helicity (for negative helicity the images have to be viewed in a mirror). **(a)** Sunspot whorls: spiral pattern of chromospheric fibrils (Hale, 1925; Nakagawa et al., 1971; Chae et al., 2001). **(b)** Vector magnetograms: the presence of magnetic helicity induces a systematic rotation of the observed field compared with the potential state. (Hagyard et al., 1990; Metcalf et al., 2005). **(c)** “Magnetic tongues” in emerging active regions: the asymmetric distribution of the B_n component is interpreted as the contribution of the azimuthal field component of an emerging twisted flux rope (López Fuentes et al., 2000; Green et al., 2007). **(d)** Shift of the flare ribbons along the inversion line. In some flares, two J-shaped ribbons are anti-symmetrically located on both sides of the B_n inversion line : this is an indication of a coronal twist with a number of turn ≥ 1 (Moore et al., 1995; Démoulin et al., 1996). **(e)** Rotating sunspots and sheared coronal loops (Schmieder et al., 1996; Brown et al., 2003). **(f)** Soft X-ray sigmoids: the coronal trace of twisted or highly sheared field lines (Manoharan et al., 1996; Canfield et al., 1999). **(g)** Global organization of fibrils and feet/barbs, i.e. their inclination on the filament axis (Martin et al., 1994; Aulanier et al., 1998). **(h)** Coherent rotation of the magnetic field in magnetic clouds (Bothmer and Schwenn, 1998; Dasso et al., 2006).

Fig. 2. Schema showing the evolution of magnetic helicity from the convective zone to the interplanetary space. Magnetic flux tubes can cross the convective zone only if they are sufficiently twisted (left insert). After emergence through the photosphere and many transformations (via magnetic reconnection), temporary storage in the corona, the magnetic field and its helicity are launched away via Coronal Mass Ejections (CMEs) detected in the interplanetary space as ICMEs and magnetic clouds (adapted from Cheung et al., 2006).

Fig. 3. Magnetic helicity injection in an active region (AR). **(a)** Longitudinal magnetogram of AR 8375 (light/dark levels codes for positive/negative values). **(b)** Photospheric velocity ($\boldsymbol{\vartheta}_{\text{LCT}}$, arrows) deduced from Local Correlation Tracking (LCT, Section 2.2) superposed on the helicity flux density, $G_A = -2(\mathbf{A}_p \cdot \boldsymbol{\vartheta}_{\text{LCT}})B_n$, distribution (grey-level convention similar to panel (a)). **(c)** Magnetic helicity rate (dH/dt , Eq. (9) with $\mathbf{u} = \boldsymbol{\vartheta}_{\text{LCT}}$, or the shearing/twisting term in Eq. (7) with $\mathbf{v}_t = \boldsymbol{\vartheta}_{\text{LCT}}$) as deduced from LCT velocity estimations ($\boldsymbol{\vartheta}_{\text{LCT}}$). The arrows indicate the time of first detection of each CME launched from AR 8375. **(d)** Accumulated change of helicity (thick line: from the measured dH/dt , thin line: from a spline interpolation of dH/dt), and full Sun soft X-ray flux (Nindos et al., 2003).

Fig. 4. Temporal evolution of a magnetic bipole initially parallel (left panels) and perpendicular to the equator (right panels) deformed by differential rotation in the northern solar hemisphere. These bipole orientations are typical of young and decayed ARs respectively. Although the shearing motion is simple and independent of time, the helicity injection rates (lower panels) are strongly evolving, and even change of sign (shaded regions, DeVore, 2000; Démoulin et al., 2002b).

Fig. 5. Helicity injection during the emergence of an AR. The top panels show the longitudinal magnetogram evolution during the beginning of flux emergence. The “magnetic tongues” (Fig. 1c) indicate the emergence of a twisted flux tube with negative magnetic helicity, in agreement with the sign of the injected helicity (continuous line in the bottom panel, scale on the right side). H has a steeper temporal evolution than the magnetic flux (dashed line, scale on the left side, Jeong and Chae, 2007).

Fig. 6. Absolute magnetic flux of both polarities (top panels), injection rate of magnetic helicity (middle panels), and helicity injected (bottom panels) measured in two emerging ARs. The helicity injection is typically peaked, delayed by ≈ 2 days from the initial magnetic flux increase (Tian and Alexander, 2008).

Fig. 7. Injection of magnetic helicity in models of emerging twisted flux tubes. On the left column, the flux rope is simply supposed to move upward with a constant velocity (Pariat et al., 2005). On the right column, an MHD simulation of the emergence across the photosphere is realized (Cheung et al., 2005). In both cases, the helicity injection is qualitatively peaked as in emerging ARs (Fig. 6).

Fig. 8. Magnetic helicity injected in various ARs during 6 days (corresponding to their central disk passage) in function of their magnetic flux (Φ). The best-fit line (dashed) is very close to the solid line giving a flux square dependence. Most X-flare regions have helicity values above 10^{42} Mx^2 (an order of magnitude for the helicity launched in a CME, LaBonte et al., 2007).

Fig. 9. The same isolated AR followed during 3 solar rotations. The left column shows the evolution and scattering of the longitudinal magnetic field. The right column shows an helicity injection (continuous line) mostly present in the first rotation when the AR magnetic flux is increasing. The scale of the magnetic flux (sum of the absolute flux of both polarities) is on the left side, and the scale of the injected helicity is on the right side (Jeong and Chae, 2007).

Fig. 10. Comparison of maps with different methods to estimate the helicity flux density in an AR. The temporal evolution of G_A (top row, Eq. 10) and G_θ (middle row, Eq. 12) are shown for AR 9182 (left) and for a model of this AR (right). The bottom left panel shows the longitudinal magnetogram of AR 9182, with LCT velocities (arrows) and polarity labels. The bottom right panel shows the estimation of G_Φ (Eq. 13) for the model. G_A has polarities of both signs, whereas G_θ has mostly the same sign in each magnetic polarities. Similar G_A and G_θ polarities of both signs are present for AR 9182 and its model. However, assuming that the magnetic connectivity of the emerging bipole, N_2P_2 , is kept, G_Φ is everywhere positive. This shows that the negative polarity of G_θ in P_2 is fake (it is due to the relative motion of the nearby magnetic polarities, Pariat et al., 2006).

Fig. 11. **(a)** Test of the different versions of the MEF method (Section 5.3) with an ANMHD numerical simulation. The helicity rate is plotted in function of the laps of time Δt selected to compute the evolution of the magnetic field ($\partial B_n/\partial t$) from theoretical magnetograms separated by Δt . **(b,c)** Application of various versions of the MEF method to an AR. The differences in the helicity rate are smaller than in the tests with the numerical simulation (Ravindra et al., 2008).

Fig. 12. Test of the DAVE (left) and DAVE4VM (right) with an ANMHD numerical simulation. The scatter plots compare the G_A values (Eq. 10) estimated (in ordinate) to the ones computed directly from the numerical simulation (in abscissa). The quoted values in the panel top are the non parametric Spearman rank-order correlation coefficient, the Pearson correlation coefficient and the slope of the fitted straight line. The ratio of the total helicity fluxes (ratio of the estimated flux over the one computed directly from the simulation) is written at the bottom of each panel. All these measurements show much better results with DAVE4VM than DAVE (Schuck, 2008).